Wide-Band and Scalable Equivalent Circuit Model for Multiple Quantum Well Laser Diodes

A Dissertation
Presented to
The Academic Faculty

by

Jae Hong Kim

In Partial Fulfillment of the Requirements for the Degree of
Doctor of Philosophy in Electrical and Computer Engineering

Georgia Institute of Technology

August 2005

Wide-Band and Scalable Equivalent Circuit Model for Multiple Quantum Well Laser Diodes

Approved by:

Dr. Martin A. Brooke, Advisor
School of Electrical and Computer Engineering
Georgia Institute of Technology

Dr. Ali Adibi
School of Electrical and Computer Engineering
Georgia Institute of Technology

Dr. Abhijit Chatterjee
School of Electrical and Computer Engineering
Georgia Institute of Technology

Dr. Hao-Min Zhou
School of Mathematics
Georgia Institute of Technology

Dr. David Schimmel
School of Electrical and Computer Engineering
Georgia Institute of Technology

Date Approved: April 19, 2005

This dissertation is dedicated to my parents and my wife, Taehee. Their support and love have encouraged me on this long path.

ACKNOWLEDGEMENTS

I would like to express my appreciation to my thesis advisor, Prof. Martin Brooke, for his constant support throughout my Ph.D. experience. I also would like to thank Prof. Abhijit Chatterjee, Prof. David Schimmel, Prof. Ali Adibi, and Prof. Hao-Min Zhou for serving as my dissertation committee members. I am especially grateful to Yoonsu Choi, Jaemin Shin, and Cheolung Cha for their assistance in my research work.

TABLE OF CONTENTS

LIST OF FIGURES

LIST OF TABLES

SUMMARY

This dissertation presents a wide-band lumped element equivalent circuit model and a building block-based scalable circuit model for multiple quantum well laser diodes. The wide-band multiple-resonance model expresses two important laser diode characteristics such as input reflection and electrical-to-optical transmission together. Additionally, it demonstrates good agreements with the measurement results of the selected commercial discrete laser diodes. The proposed building block-based modeling approach proves its validity using a numerically derived scalable rate equation. Since success in a circuit design depends largely on the availability of accurate device models, the practical application of the proposed models provides improved accuracy, simple implementation and a short design time.

Chapter 1. Introduction

Semiconductor laser diodes have been used as the main sources of fiber-optic communication systems and optical interconnections. Since the accuracy of the circuit simulation cannot surpass the accuracy of the individual equivalent circuit models used, building an accurate laser diode model becomes more important in modern high-speed optoelectronic integrated circuit (OEIC) design. Various efforts have been made to get a well-established laser models such as a rate equation-based model and a finite-difference-time-domain (FDTD) -based model for OEIC design however, the difficulty of extracting accurate model parameters in the rate equation-based model case and the long simulation time in the FDTD-based model remain major obstacles to applying them to actual OEIC design.

Motivated by these observations, this dissertation presents a measurement-based small-signal multiple resonance lumped-element model for ready-made laser diodes. Important laser characteristics, such as input reflection and electrical-to-optical transmission, the main concerns of circuit designers, are expressed together over a broad frequency range. A simple model implementation process and short simulation time demonstrate its usefulness.

Although the lumped element modeling for ready-made laser diodes meets some needs of circuit designers, it does not satisfy the needs of changing the laser diode geometry to allow circuit design engineers to have more control over the circuit design. In this

respect, a broadband building block-based scalable laser diode model is also proposed. Originally, we intended to use Microelectronic Research Center (at Georgia Tech) fabricated ridge wave-guide laser diodes for this scalable laser diode modeling; unfortunately, the obtained devices did not show reasonable AC performance. Thus, we derived a cavity length scalable rate equation numerically, and constructed a building block-based scalable model. The comparison of simulation results confirmed the effectiveness of the proposed methodology in scalable laser modeling.

Chapter 2 gives a brief background of laser diode operation and various types of laser equivalent models. Two proposed laser models are fully explained in Chapter 3, and finally, Chapter 4 summarizes the conclusion of this work.

Chapter 2. Background and the Types of Laser Diode Models

2.1. Edge-Emitting Laser Diode Properties

2.1.1. Laser Diode Structures and Operating Principles

When a voltage is applied to a degenerated *pn* junction device, considerable electrons and holes are injected into the transition region. If the bias is large enough, the transition region contains a high concentration of conduction band electrons and a high concentration of valence band holes as shown in Figure 2.1. In other words, a population inversion exists around the junction. This population inversion region is also called the active region. As the current is increased to the level of significant population inversion, the stimulated emission of radiation (i.e., highly directional, monochromatic, coherent light emission) starts.

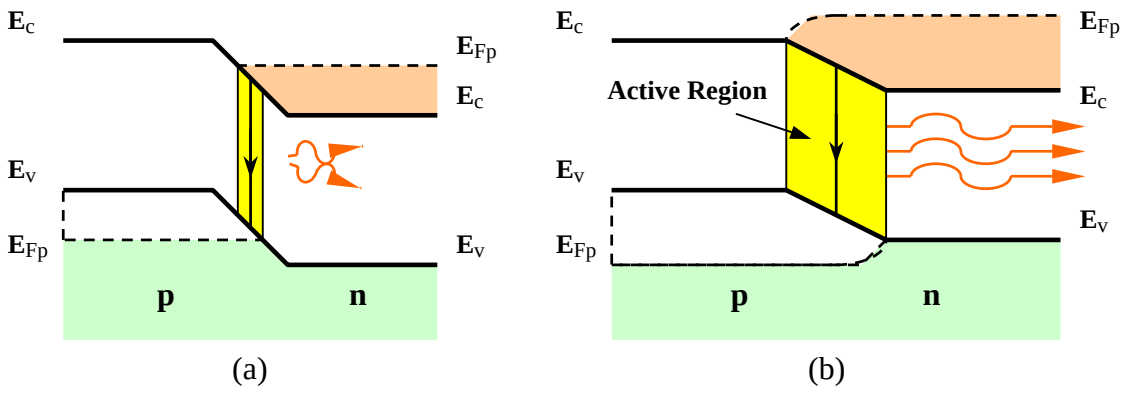

Figure 2.1 The formation of population inversion: (a) under weak forward bias, and (b) under strong forward bias.

Another condition to sustain continuous laser operation from the device is the optical cavity. Its main function is to implement a laser oscillator, or to build up the intensity of stimulated emissions by means of an optical resonator.

In a semiconductor laser, cleaving two ends of the laser diode chip will form mirror facets. Initial light output begins because of spontaneous transitions between conduction band and valence band, and this small amount of light output is selectively amplified in the cavity between the two mirrors. Since only multiples of the half-wavelength can exist in an optical cavity, the radiation wavelength that can build up in the cavity is determined by the cavity length L,

$$L = m\frac{\lambda_0}{2n}, \tag{2.1}$$

where m is an integer, λ_0 is the free space wavelength, and n is the refractive index of the semiconductor. The resonant frequency of the cavity, i.e., a mode of cavity, satisfies the above relationship.

The device described thus far is a homo-junction laser, since both *p* and *n* regions are fabricated with the same semiconductor. The drawback is that it is difficult to have a well-defined active region and mode volume thickness. This means that homo-junction lasers cannot be continuously operated at room temperature. To overcome this limitation, a hetero-junction structure is used (Figure 2.2).

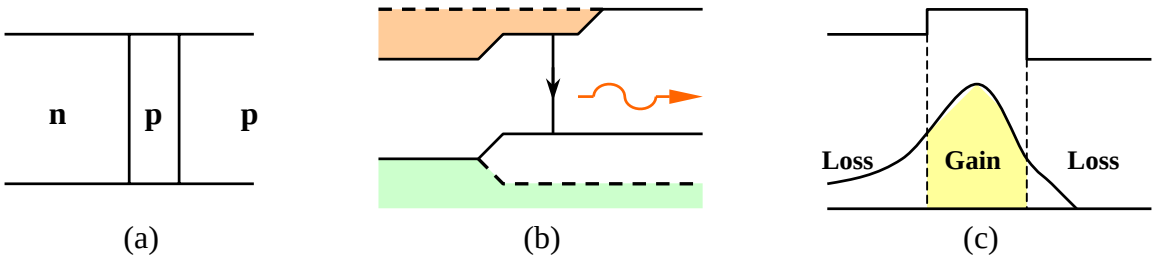

Figure 2.2 **Hetero-junction structure; (a) layer structure, (b) band diagram, and (c) optical confinement.**

The injected carriers are confined to a narrow region so that population inversion can be built up at lower drive current levels. In addition, the refractive index change at the hetero-junction provides a better optical confinement of the photons.

Further improvements in laser performance are possible by introducing a quantum well structure. A typical single quantum well device has an ultra-thin narrow band-gap material sandwiched between two wider band-gap materials (Figure 2.3a). The electron concentration at E_1 increases rapidly without the need for a large current injection; hence, population inversion occurs quickly. Another advantage is that it has a narrow line width in the output spectrum since the majority of the electrons stay at or near E_1 and holes stay at or near E_1', the range of emitted photon energies are very close to E_1 - E_1'. The multiple quantum well structure schematically sketched in Figure 2.3 extends the advantages of the single quantum well laser. It is composed of alternating ultra-thin layers of wide and narrow band-gap semiconductors. The narrow band-gap layers play the active layer parts where electron confinement and lasing transition take place and the wide band-gap layers provide the barrier layer parts.

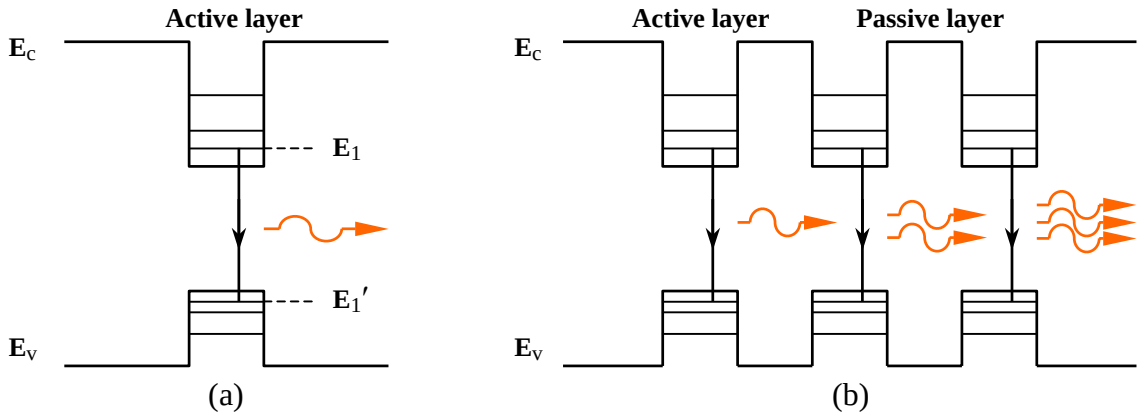

Figure 2.3 Quantum well structure band-gap diagram; (a) single quantum well laser and (b) multiple quantum well laser.

Finally, the introduction of compressive strain into the multiple quantum well lasers leads to low internal loss, high quantum efficiency, low threshold current operation, and small line-width enhancement factors [1-3].

2.1.2. Light Output and Current Relationship

For a better understanding of semiconductor laser diode operation, let us discuss the light output-current (L-I) relationship, one of the important laser characteristics.

In the region below the threshold steady state, the generation rate equals the recombination rate,

$$\frac{\eta_i I_{th}}{qV} = (R_{sp} + R_{nr} + R_l)_{th} = \frac{N_{th}}{\tau}. \qquad (2.2)$$

The left term represents the generation term, $\eta_i I/q$ electrons per second being injected to the active region V, and the right term represents the recombination term such as the spontaneous recombination rate R_{sp}, the nonradiative recombination rate R_{nr}, and the carrier leakage rate R_l. Above the threshold, the recombination rate will be clamped at its threshold value.

In the region above the threshold condition, the photon density equation is given as below:

$$\frac{dN}{dt} = \frac{\eta_i I}{qV} - \frac{N}{\tau} - v_g g N_p, \qquad (2.3)$$

where v_g is the group velocity and g is the gain per unit length. If we substitute Equation 2.2 into the above photon density equation, a new above-threshold photon density equation is obtained:

$$\frac{dN}{dt} = \eta_i \frac{(I - I_{th})}{qV} - v_g g N_p. \qquad (I > I_{th}) \qquad (2.4)$$

Now we can calculate a steady-state photon density above the threshold condition:

$$N_p = \frac{\eta_i (I - I_{th})}{q v_g g V}. \qquad \text{(at steady state)} \tag{2.5}$$

The optical output is constructed as the multiplication of stored optical energy in the cavity and the energy loss rate through the mirrors as shown in equation (2.6).

$$L_O = v_g \alpha_m N_p h\nu V_p, \tag{2.6}$$

where hν is the energy for photon, V_p is the cavity volume, and $v_g\alpha_m$ is the energy loss rate through the mirrors. By defining the average internal loss $< \alpha_i >$ and the mirror loss α_m, the equation is written as $\Gamma g_{th} = < \alpha_i > + \alpha_m$ using $\Gamma = V/V_p$; then Equation 2.6 can be rewritten as

$$L_O = \eta_i \left(\frac{\alpha_m}{\langle \alpha_i \rangle + \alpha_m} \right) \frac{h\nu}{q} (I - I_{th}). \qquad (I > I_{th}) \tag{2.7}$$

By applying another definition $\eta_d = \eta_i\alpha_m/(< \alpha_i > + \alpha_m)$, Equation 2.7 can be simplified as

$$L_O = \eta_d \frac{h\nu}{q} (I - I_{th}). \qquad (I > I_{th}) \tag{2.8}$$

This equation shows that the light output power above the threshold is a linear function of the current above the threshold (Figure 2.4).

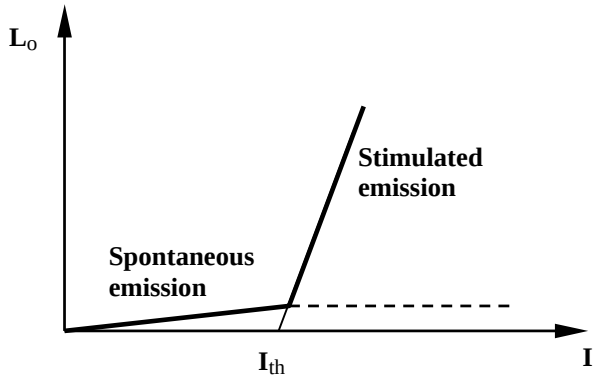

Figure 2. 4 Light output vs. current (L-I) relationship.

The differential quantum efficiency, defined as the number of photons out per electron, can be measured by finding the slope $\Delta L_O/\Delta I$ in watts/ampere in the above-threshold region.

2.1.3. Temperature Dependence

The laser diode output characteristics tend to be temperature sensitive. Figure 2.5 displays optical output power changes along the laser diode driving current input with the case temperature.

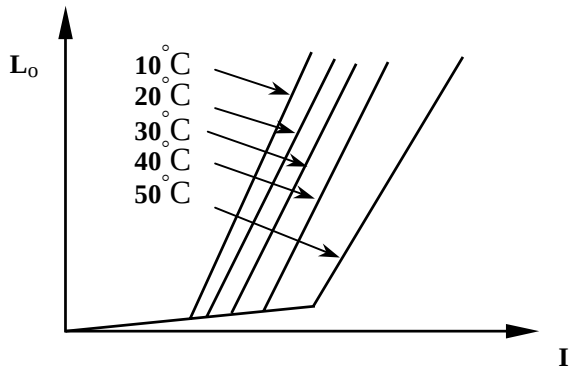

Figure 2.5 Light output power vs. driving current at different temperatures.

As the temperature increases, the threshold current shows a steep increase, typically as the exponential of the absolute temperature. The output spectrum also moves with the temperature changes. For example, the peak emission wavelength of a single-mode laser diode exhibits "jumps" at certain temperatures. This jump corresponds to a "mode hop" in the output. This phenomenon can be interpreted as another mode at a different operating temperature fulfilling another laser oscillation condition, which refers to a discrete change in the oscillation wavelength. As mode hopping is undesirable phenomenon in almost all applications, thermoelectric coolers are usually integrated into the laser package to control device temperature.

Temperature dependence is especially strong in InGaAsP lasers used for optical communications because the efficiency of Auger recombination increases with the reduced band-gap. Active region carrier leakage is also believed to be a reason for strong temperature dependence.

2.2 Physics-Based Laser Diode Models

2.2.1 Rate Equation Method

One of the prevailing laser diode models is based on a set of rate equations. The rigorous derivation of these equations originates from Maxwell equations with a quantum mechanical approach for the induced polarization [4]. However, the rate equation could also be derived by considering physical phenomena [5].

$$\frac{dN}{dt} = \frac{\eta_i I}{qN_w V_{act}} - R_w(N) - \Gamma_c v_{gr} \frac{\alpha(N)}{\phi(S)} S , \tag{2.9}$$

$$\frac{dS}{dt} = -\frac{S}{\tau_p} + N_w R_{w\beta}(N) + N_w \Gamma_c v_{gr} \frac{\alpha(N)}{\phi(S)} S , \tag{2.10}$$

$$\frac{S}{P_f} = \frac{\lambda \tau_p}{\eta_c V_{act} hc} = \vartheta . \tag{2.11}$$

Equation 2.9 relates the rate of change in carrier concentration N to the drive current I, the carrier combination rate $R_w(N)$, and the stimulated emission rate S. Equation 2.10 relates the rate of change in photon density S to photon loss, the rate of coupled recombination into the lasing mode, and the stimulated emission rate. The photon density S to the output power P_f is described in Equation 2.11.

In the case of practical circuit design application, the above equations go through additional rearrangements and the introduction of several definitions. While the detailed and lengthy procedures are omitted, Figure 2.6 shows the final equivalent circuit model.

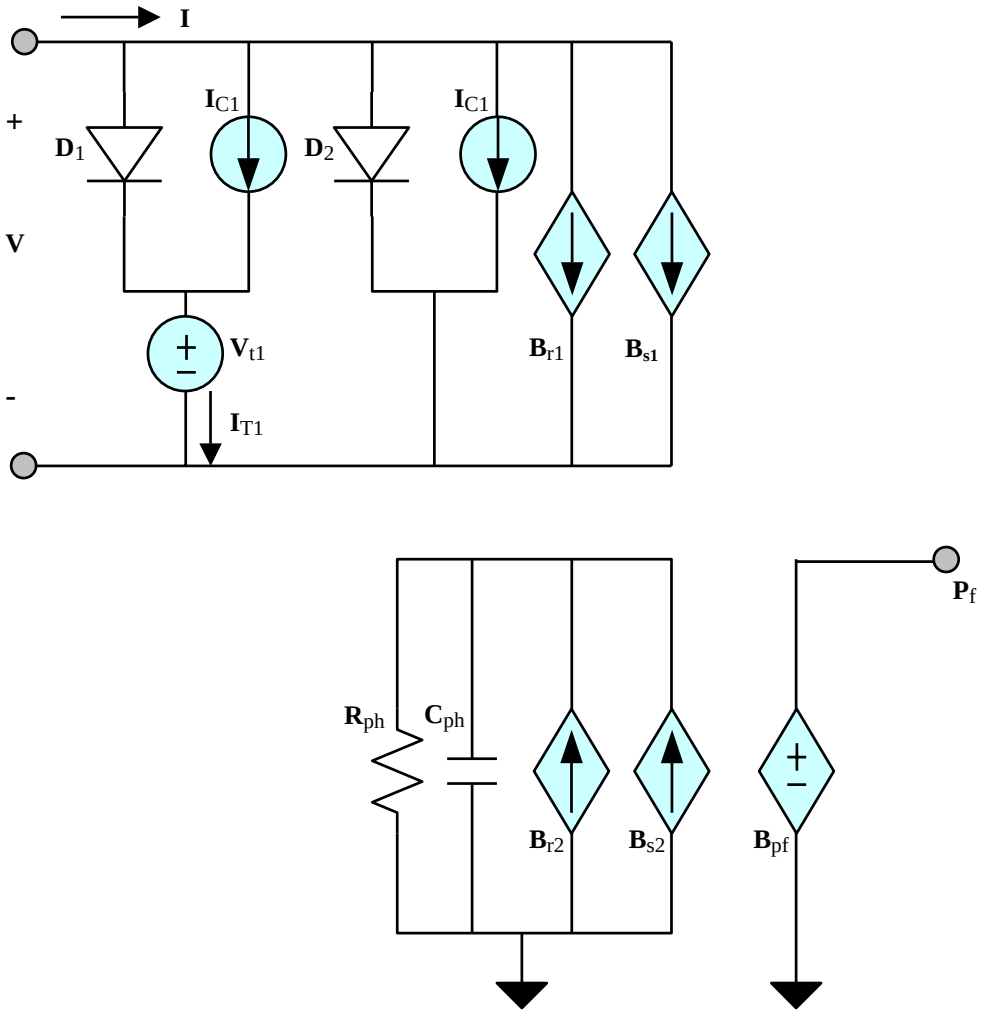

Figure 2.6 Simple equivalent circuit model for a quantum well laser diode.

The parameters and their values to build the equivalent circuit model are presented in Table 2.1.

Table 2.1 Parameters to build the equivalent circuit model in Figure 2.6, the values are taken from [6].

Parameter	Description	Value
η_i	Current injection efficiency	0.86
λ	Emission wavelength	980nm
N_w	Number of quantum well	1
V_{act}	Volume of one quantum well	6×10^{-18} m^3
Γ_c	Optical confinement factor of one QW	0.019
ν_{gr}	Lasing medium group velocity	8.571×10^{7} m/s
τ_p	Photon lifetime	2.759 ps
η_c	Output power coupling coefficient	0.449
N_0	Optical transparency density	1.5×10^{18} cm^{-3}
G_0	Gain coefficient per quantum well	1500 cm^{-1}
ε	Phenomenological gain saturation term	1×10^{-17} cm^3
A	QW uni-molecular recombination rate coefficient	1.1×10^{8} s^{-1}
B	QW radiative recombination rate coefficient	0.7×10^{-10} cm^3/s
C	QW Auger recombination rate coefficient	0.6×10^{-29} cm^6/s
A_b	SCH unimolecular recombination rate coefficient	1.3×10^{8} s^{-1}
B_b	SCH adiative recombination rate coefficient	1.4×10^{-10} cm^3/s
C_b	SCH Auger recombination rate coefficient	1.3×10^{-29} cm^6/s
β_A	Unimolecular recombination coupling term	0
β_B	Radiative recombination coupling term	1×10^{-4}
β_C	Auger recombination coupling term	0
V_{barr}	Volume of SCH layer	2.25×10^{-16} m^3
τ_{capt}	Quantum well capture lifetime	45 ps
τ_{em}	Quantum well emission lifetime	400 ps

Rate equations have various levels of complexity to express more accurate laser operations. The above model is one of the simpler equivalent circuit models. In other words, more complex equations and many parameters are required to improve model performance.

The main problem with the rate equation based model is that circuit designers need to know the physical fabrication parameters of the laser, which includes the number of quantum wells and the volume of one quantum well. Although laser manufacturers provide such data, it is typically limited and insufficient for the circuit design. In addition, the remaining parameters still need a lot of measurement facilities and a long measurement time. Consequently, a considerable computational burden could be imposed using differential equations and exponential functions in the model. For example, the current in the diode D2 is shown below:

$$I_{D2} = \frac{qN_w V_{act} N_e}{2\eta_i \tau_n}\left[\exp\left(\frac{qV}{nkT}\right) - 1 + \frac{2q\tau_n}{nkT}\exp\left(\frac{qV}{nkT}\right)\frac{dV}{dt}\right]. \qquad (2.12)$$

Finally, rate equation based models could have an advantage in expressing nonlinear characteristics like near threshold operation: they are critical for OEIC design due to the slow speed and signal distortion from operation in the nonlinear region.

2.2.2 Finite-Difference-Time-Domain (FDTD) Method

Another physics based laser diode modeling technique uses finite-difference-time-domain (FDTD) method, which is a popular electromagnetic modeling technique. The FDTD belongs in the class of differential time domain numerical modeling methods.

In the semiconductor laser diode modeling area, the physically based FDTD device model predicts the electrical characteristics associated with specified physical structures and bias conditions. First, two- or three-dimensional mesh, consisting of numerous nodes, is setup to approximate the real operation of a laser diode as shown in Figure 2.7.

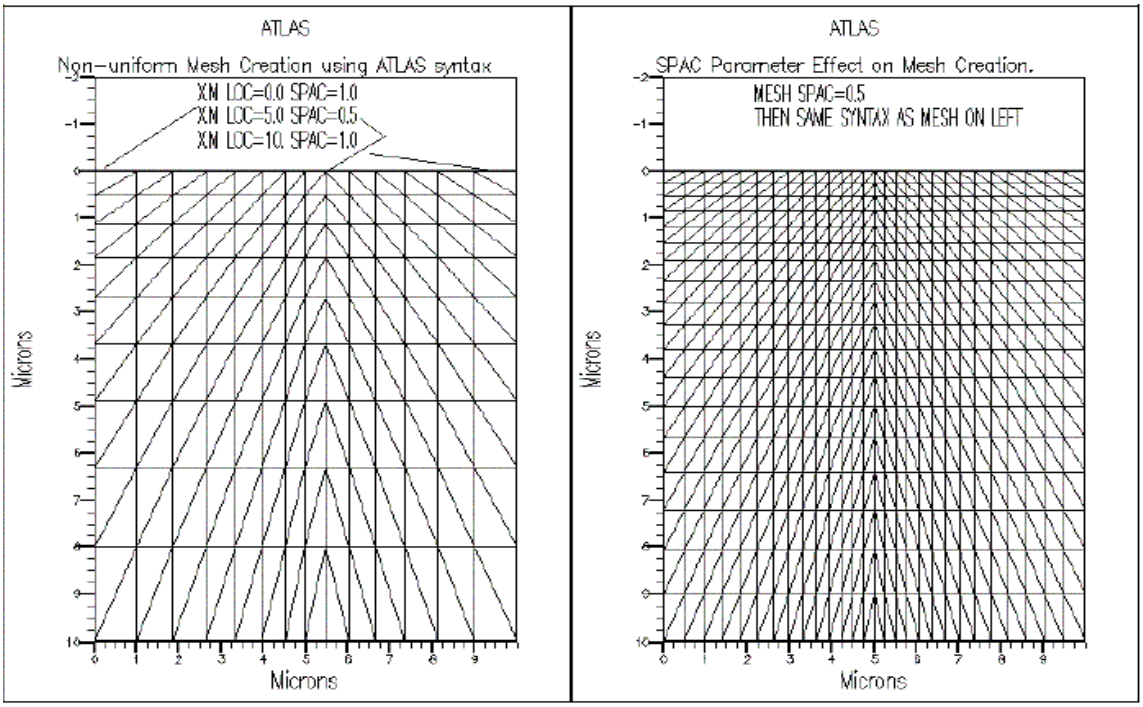

Figure 2.7 A mesh example from the commercial software, Silvaco ATLAS [7].

To simulate the semiconductor laser diode using physics-based numerical method, at least four kinds of partial differential equations are necessary. They are the Poisson equation for the electrostatic potential, the continuity equation for the carrier transportation, the vector Helmholtz equation for the optical field, and the photon rate equation for the stimulated light output. There are many systematic approaches to solve the laser diode operation numerically [8-11]. A general procedure to reach a solution is explained in the following way. First, a simulator solves the Poisson equation for the given device conditions and generates potential. Second, the potential obtained is substituted into the continuity equations for holes and electrons. Third, it solves the Helmholtz equation to obtain optical profile, and fourth, using the iterative calculation with the photon rate equation, the tool solves for the individual photon-numbers in the cavity, This procedure is repeated for convergence at an initial bias point and the device is recalculated for the next bias point.

Several literatures established those laser diode operation governing equations [12-14], so the explanation on each partial equation will be given only briefly as below.

The electronic part of the laser diode operation can be solved using Poisson equation, which is given by

$$\nabla \cdot (\nabla \phi) = -\frac{\rho}{\varepsilon} \tag{2.13}$$

where ϕ is the electrostatic potential, ρ is the charge density, and ε is the permittivity.

This is the generalized Laplace's equation ($\nabla\cdot(\nabla\phi)=0$), one of the important and basic partial differential equations. The usual charge density expression and the relationship between the potential ϕ and the hole and electron concentrations are

$$\rho = q\left(N_d^{+} - N_a^{-} + p - n\right) \tag{2.14}$$

$$p = p_0 \cdot e^{-q\phi/kT} \tag{2.15}$$

$$n = n_0 \cdot e^{q\phi/kT} \tag{2.16}$$

where N_d^+ and N_a^- are the ionized donor and acceptor concentrations, respectively. P_0 and n_0 are the equilibrium concentration of holes and electrons. Solving the Poisson equation with the given conditions generates the potential profile in the presence of electrical charges.

The electronic equations are coupled into the optical part by the recombination terms in the continuity equations:

$$-\nabla \cdot J_p = q\frac{\partial p}{\partial t} + q\left(R^{nr} - G\right) \tag{2.17}$$

$$\nabla \cdot J_n = q\frac{\partial n}{\partial t} + q\left(R^{nr} - G\right) \tag{2.18}$$

where R^{nr} is the non-radiative recombination rate such as SRH and Auger recombination, and G the generation rate.

The wave equation for the electric field in the cavity of an edge-emitting laser diode can be described as follow:

$$\nabla \times \nabla \times E = -\mu_0 \left(\sigma \frac{\partial E}{\partial t} + \varepsilon_0 \varepsilon_r \frac{\partial^2 E}{\partial t^2} + \frac{\partial^2 P}{\partial t^2} \right) \tag{2.19}$$

where E is the electric field, σ is the conductivity, ε_r is the electric permittivity, and P is the polarization due to spontaneous recombination of electron-hole pairs.

Under the condition of the transverse 2-D cuts and a longitudinal 1-D situation, the spatial optical equations are expressed with the vector Helmholtz equation as follows:

$$\left(\frac{\partial^2}{\partial x^2} + \frac{\partial^2}{\partial y^2} \right) \Phi + k_0{}^2 \left(\varepsilon_{xyz} - \varepsilon_z \right) \Phi = 0 \tag{2.20}$$

$$\frac{\partial^2}{\partial z^2} \Psi + k_0{}^2 \left(\varepsilon_z - \xi \right) \Psi = 0 \tag{2.21}$$

ε_{xyz} denotes the relative combined permittivity at the optical frequency, which can include material gain

$$\sqrt{\varepsilon_{xyz}} = n(x,y,z) + \frac{ic}{2\omega_0} \left(r^{st}(x,y,z) - \alpha(x,y,z) \right) \tag{2.22}$$

with the refractive index n, local material gain r^{st}, and free carrier absorption α.

Introducing the photon number $S(t) = \frac{\varepsilon_0 \bar{\varepsilon}_r}{\hbar \omega_0} E(t)^2$, the photon rate equation is obtained as follow:

$$\frac{\partial S}{\partial t} = \left(\frac{2\bar{\sigma}}{\varepsilon_0 \bar{\varepsilon}_r} + \frac{\omega_0 \xi''}{\bar{\varepsilon}_r} \right) S + \frac{c}{\sqrt{\bar{\varepsilon}_r}} R^{sp} \tag{2.23}$$

where $R^{sp}(t)$ is the spontaneous emission into the considered cavity mode.

The partial differential equations are simply modified to central difference equations, discritized, and implemented in software code. And then, the equations are solved in a leapfrog manner to the end of calculation time. Through this procedure, it is possible to simulate the carrier transportation through a semiconductor laser diode structure or the electrical performance of a laser can be modeled in DC, AC or transient mode of operation.

To use FDTD method a computational domain should be established. The electro-magnetic field will be calculated at every point within the computational domain. Since FDTD requires that the entire computational domain be gridded, and these grids should be small compared to the smallest wavelength and smaller than the smallest feature in the model. Very large computational burden cannot be avoided. Models involving several partial differential equations like a laser diode model need excessively large computational time. For example, one of the general laser physics simulation software, Silvaco ATLAS, takes several days to obtain reasonable laser operation responses.

Physically based FDTD laser diode modeling has two advantages. It can provide insights in the level of device physics, which is useful for laser device fabrication engineers, and it can also provides information that is difficult or impossible to measure. However, this method suffers several limitations. First, modeling engineers should know the exact physical structure, which is impossible in most cases. Second, it needs very long simulation time. Because FDTD requires that the entire computational domain be meshed small enough, very large computational domains should be established to get an accurate

response. Actually some of my simulation trials showed that it could take six hours for a simple structure and several days for a complex structure. Lastly, FDTD finds the electro-magnetic fields directly everywhere in the computational domain; thus, considering the field profile beyond the laser output facet will force the computational domain to be excessively large. As a result, it increases the simulation time additionally.

In terms of computational burden, the lumped-element equivalent circuit model can significantly lower calculation load. The main reason comes from the fact that the model consists of linear components only like a resistor, inductor and capacitor (RLC). Although capacitors and inductors introduce time derivative terms into the circuit, they cause just linear differential equation terms. The analytical solutions for the linear circuits can be easily obtained with a simple algebraic equation substitution using Laplace transform technique. The actual implementation in the commercial circuit simulator such as a SPICE uses nodal analysis approach [15, 16]. It first arbitrary label every node in some order then continue to label every element whose current is one of the outputs. Capacitances and inductances are considered only in the time domain and their contributions are obtained by applying finite differencing methods to their branch relations. The consecutive nodal matrix manipulation and calculation generates the circuit response.

2.3 Circuit-Level Laser Diode Models

2.3.1 Small-Signal Equivalent Circuit Model

Laser rate equations with the time derivatives, as shown in Equations 2.9 and 2.10, should be analyzed to ascertain the dynamical behavior of the laser diode to a perturbation such as a modulation of the current. Unfortunately, exact analytical solutions to the full rate equations cannot be obtained. Therefore some approximations are needed to find analytical solutions. It is possible to assume that the dynamic changes in the carrier and photon densities away from their steady-state values are small. Under this assumption, the small-signal responses of one variable in terms of a perturbation to another can be expressed by taking the differential rate equations.

For example, Salehi *et al*. assumed small-signal perturbation condition on a set of the single mode rate equations [17] as follows:

$$I(t) = I_0 + i \cdot \exp(j\omega t), \tag{2.24}$$

$$N(t) = N_0 + n \cdot \exp(j\omega t), \tag{2.25}$$

$$S(t) = S_0 + s \cdot \exp(j\omega t), \tag{2.26}$$

where I_0, N_0, and S_0 are the steady state solutions, and *i*, *n*, and *s* are the magnitudes of the corresponding small-signal perturbations. DC bias voltage $V_j(t)$, optical gain $G_m(t)$, trap density $T(t)$, and average light power $P_{avg}(t)$ are defined in the same manner. By applying several numerical operations, derivations of coefficients, and separations of the terms that contain $exp(j\omega t)$ yields

$$j\omega C_n v_j = i - g'\Delta p - \frac{v_j}{R_{S1}} - \frac{v_j}{R_{S2}} - j\omega C_T v_j \,, \tag{2.27}$$

$$j\omega C_{op}\Delta p = \alpha_{sp}\Delta i_{sp} + \alpha_{st}\Delta i_{st} - \frac{\Delta p}{R_l} - \frac{\Delta p}{R_T} + K_T v_j \,. \tag{2.28}$$

The detailed explanations are omitted. The final small-signal equivalent circuit model is obtained using Equations 2.27 and 2.28. Figure 2.8 shows circuit level laser model.

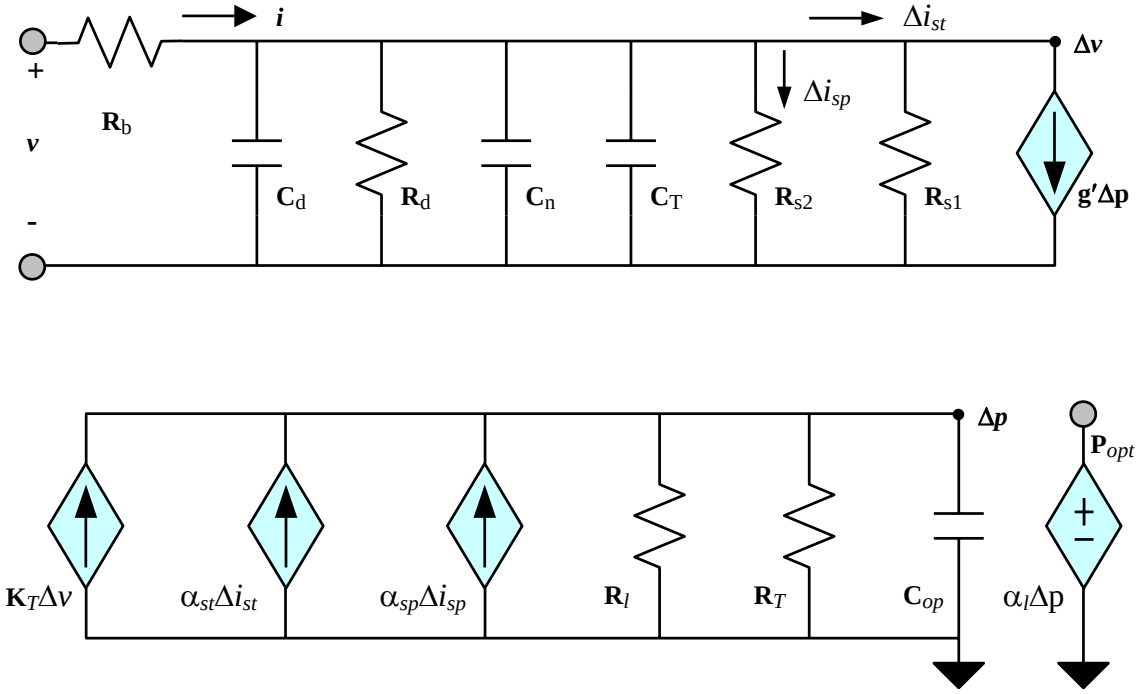

Figure 2.8 An example of small-signal equivalent circuit model.

The upper part of the above schematic shows an input electrical equivalent circuit model, and the lower part of the schematic displays an optical equivalent circuit model, where the photon density depends on density of the electrical carriers.

Although this model has the significant features of including the influence of substrate and package parasitics, and it facilitates the inclusion of device-circuit interactions in calculated response characteristics. These kinds of small-signal models need the physical parameters of the laser diodes. Thus, the parameters for the equivalent circuit in Figure 2.8 should be known before making a model. Table 2.2 summarizes the parameters.

Table 2.2 Parameters for the example equivalent model in Figure 2.8.

Parameter	Description	Value
V_{qw}	Volume of the quantum well	23.425 μm^3
λ	Wavelength	980 nm
α_I	Intrinsic loss	11.8 cm^{-1}
B	Band-to-band recombination coefficient	3.4×10^{-11} cm^3s^{-1}
β	Spontaneous emission coupling coefficient	9.8×10^{-4}
R	Reflectivity	0.3
E_{qw}	Energy of the quantum well	1.482 eV
R_b	Series resistance	4 Ω
Γ	Optical confinement factor	0.187

2.3.2 Large-Signal Equivalent Circuit Model

If semiconductor lasers are biased below or close to the threshold level, modulation depth does not satisfy the valid criterion, that is, the small perturbation *i* is not much smaller than the steady state current I_0, then the linear system approximation is impossible. To decide the dynamic response of the laser diode under the condition of large-signal inputs, the general rate equations 2.9 and 2.10 should be used. They are valid below the threshold region and above the threshold region.

One of the large signal model approaches was implemented using the Hewlett Packard Advanced Design System (HP-ADS) symbolically defined devices (SDDs) model to 1.3 μm InGaAsP/InP Fabry-Perot lasers [18-20]. They claimed the model enables the simulation of the transient and steady state dynamic performance of the given laser diodes including carrier concentration, photon density, optical power level, and phase response. The SDD is an equation-based component that enables for engineers to define non-linear, custom components easily. Specifying device operation equations that relate port voltages, port currents, and their derivatives is a core part of the actual implementation of the SDD. The benefits of the SDD is that once a model is defined, any circuit simulator in Advanced Design System can use the model, and derivatives are also calculated automatically in the process of simulation. They modified the normalized laser model given in [18] by introducing the effects of the noise sources and the phase term into the rate equation. The modified rate equations are as follows:

$$\frac{dP_n(t)}{dt} = \frac{(C_n - C_{tr}{}^n)}{\tau_{ph}(1 - C_{tr}{}^n)} \frac{P_n}{\sqrt{1 + P_r{}^n}} - \frac{P_n}{\tau_{ph}}$$

$$+ \left(\beta_{sp} B_0 C_{tho} \tau_e e^{\left(\frac{T - T_r}{T_0} - \frac{E \cdot q}{k \cdot T} \right)} \right) C_n{}^2 + F_{P_n}(t) \qquad (2.29)$$

$$\frac{dC_n(t)}{dt} = \frac{I_{eff}(t)}{qV_c C_{th}} - \frac{(C_n - C_{tr}{}^n)}{\tau_e \cdot \tau_{ph}(1 - C_{tr}{}^n)} \cdot \frac{P_n}{\sqrt{1 + P_r{}^n}}$$

$$- \frac{C_n}{\tau_e} + F_{C_n}(t) \qquad (2.30)$$

$$\frac{d\phi_n(t)}{dt} = \frac{\beta}{2} \cdot G_n \cdot (C_n - \overline{C_n}) + F_{\phi_n}(t) \qquad (2.31)$$

The above equations include the relationships below.

$$C_n = \frac{C}{C_{th}} \qquad (2.31), \qquad C_{tr}{}^n = \frac{C_{tro}}{C_{tho}} \qquad (2.32)$$

$$C_{tho} = \left(C_{tro} + \frac{1}{\Gamma \cdot v_g \cdot \tau_{ph} \cdot \wp_0} \right) \qquad (2.33)$$

$$P_n = \frac{P \cdot \tau_e}{\Gamma \cdot C_{th}} \qquad (2.34), \qquad P_r{}^n = \frac{P_n}{P_s{}^n} \qquad (2.35)$$

$$P_s{}^n = \frac{\tau_e}{\Gamma \cdot C_{th}} P_s \qquad (2.36), \qquad P_s = \frac{\varepsilon_0 \cdot \overline{n} \cdot n_g}{\Gamma \cdot \omega_0 \cdot \hbar} I_s \qquad (2.37)$$

P represents the photon density, *C* represents the active region carrier density, C_{tho} gives the threshold carrier number at room temperature, C_{tro} gives the transparency carrier number at room temperature, and the mean of the carrier number is expressed by $\overline{C}$.

The three-port symbolically defined device model schematic is implemented and shown in Figure 2.9, and the designated equations and their variables are presented in Figure 2.10. The input current drives the port 1, the corresponding carrier density in the active region is calculated in the port 3, and then the photon density in the port 2 is derived from the input driving current and the carrier density. It is noteworthy that this model relates port currents, port voltages, and their derivatives simultaneously.

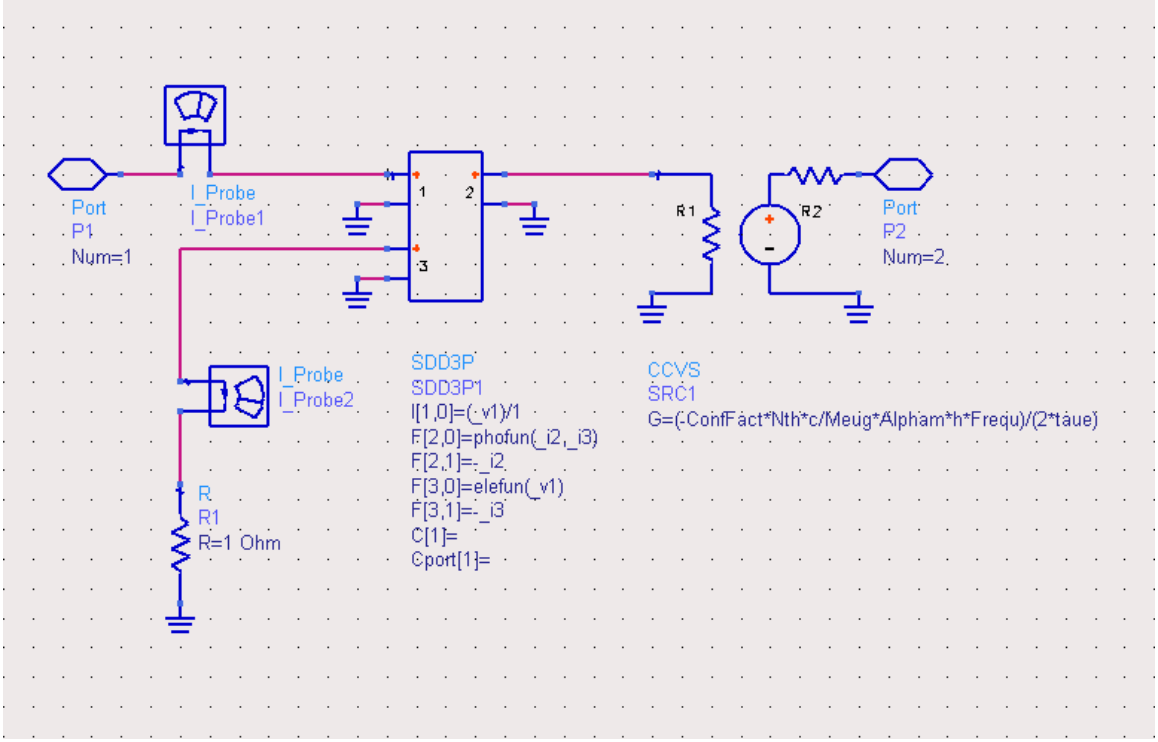

Figure 2.9 The schematic of the SDD implemented laser diode model.

```
Var Eqn VAR
VAR1
pn=_i2                                          curr1=0
nn=_i3                                          lact=if (Currfun<0) then curr1 else currf endif
ntr=n0*exp((T-300)/T0)                          lactn=lact/(ConfFact*qelect*Vol*nthr)
ntho=n0+1/(ConfFact*(c/Meug)*taup*DiffGain)     currf=Io*(exp(((Currfun-Vo)*qelect)/(k*T))-1)
nthr=ntho*exp((T-300)/T0)                       YY=sqrt(1+pn/psn)*(1-ntrn)
taue=1/(Anr+B0*nthr+Ca*nthr*nthr)               GT=((nn-ntrn)*pn)/YY
Nth=nthr*Vol                                    fun1(lact)=lactn-nn/taue-GT/(taue*taup)
Ith=qelect*Nth/taue                             elefun(lact)=fun1(lact)
taup=1/((c*(Alpham+AlphaInt))/Meug)             termsp=Kroom*exp((T-300)/T0-(E1*qelect/(k*T)))
ntrn=n0/ntho                                    phofun(pn,nn)=GT/taup-pn/taup+nn^2*termsp
Kroom=Betas*1.395e-16*Vol*ntho                  Frequ=c/Lambda
Currfun=_v1
Is=(h^2)/(4*PI^2*dipmom^2*tauln*(tauc+tauv))
ps=(Epso*Meu*Meug*Is)/(h*Frequ*ConfFact)
psn=(taue*ps)/(ConfFact*nthr)
```

Figure 2.10 The variables nomination of the SDD implemented laser diode model.

Figure 2.11 shows that this model can simulate the performance of direct modulation.

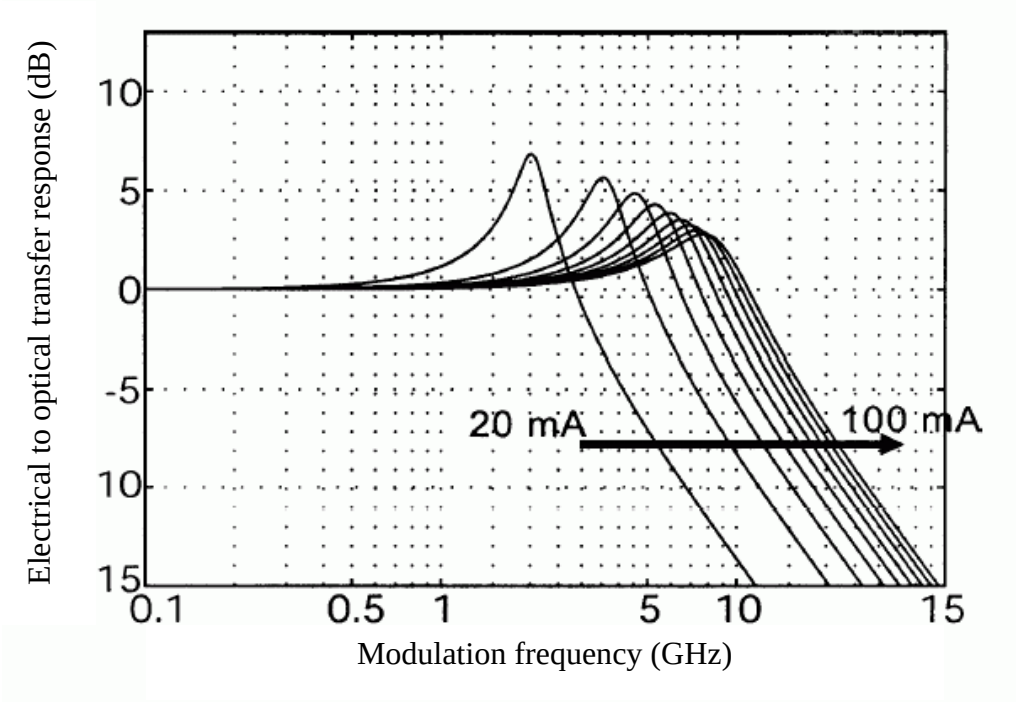

Figure 2.11 The electrical-to-optical transfer response of the directly modulated laser diode.

Table 2.3 summarizes other parameter names and their descriptions. General parameters such as Boltzmann's constant (k), electronic charge (q), permittivity of free space (ε_0), Plank's constant (h), and speed of light (c) are omitted for convenience.

Table 2.3 Device parameters for InGaAsP/InP laser diodes [18-20].

Parameter	Description	Value
L	Active region length	250 μm
W	Active region width	2 μm
d	Active region thickness	0.2 μm
λ	Operating wave length	1.3 μm
C_{tro}	Transparency carrier density	1×10^{24} m^{-3}
R1	Reflectivity factor of front facet	0.3246
R2	Reflectivity factor of front facet	0.3246
Γ	Mode confinement factor	0.3
$\overline{n}$	Effective mode index	3.5
n_g	Group refractive index	4
β	Line with enhancement factor	5
$\wp_0$	Differential gain coefficient	2.5×10^{-20} m^2
A_{nr}	Nonradiative recombination rate	1×10^{8} S^{-1}
B_0	Radiative recombination coefficient	1×10^{-16} m^3/S
C_{ao}	Auger recombination coefficient	3×10^{-41} m^6/S
d_m	Dipole moment	9×10^{-29} C·m
τ_{in}	Dipole relaxation time	0.1×10^{-12} S
τ_c	Electrons interaband relaxation time	0.3×10^{-12} S
τ_v	Holes interaband relaxation time	0.07×10^{-12} S
β_{sp}	Spontaneous emission factor	10^{-4} - 10^{-5}
T_0	Active region characteristic temperature	70 °K

One example of the large signal equivalent circuit models is presented in this section. They claimed that their model is the first one that includes thermal effects, leakage current, and noise effects simultaneously in their enhanced set of laser rate equations [20]. It is desirable that the model can include various noise evaluations such as laser relative intensity noise (RIN), frequency noise spectrum (FNS), and line-width Δf simulations.

Although their approach has several advantages, the modified rate equations still require many physical parameters, as shown in Table 2.3, and the extended equations cannot be solved analytically; thus, applying a numerical algorithm to the calculation process is inevitable. This step is possible by iterating from one rate equation to the next step using a small increment of time Δt in place of dt. It results in a considerable simulation time increase. Besides the limitations such as the need of physical parameters and long calculation time, the other critical disadvantage is that it does not include appropriate procedure for implementing the input reflection responses in the model. Since the system performance enhancement, such as dynamic range improvements and signal distortion reduction cannot be realized without including correct input reflection responses, omitting this aspect of a laser device could be a tremendous obstacle in the actual circuit design application.

2.3.3 Macromodels

One of the major methodologies for integrating the device behavior into circuit simulation tools is the macro-modeling approach. We can consider the macromodel as a black box which captures the device behavior at the input and output ports. Using the rational function, the frequency response *H(s)* of any linear time-invariant network can be represented as:

$$H(s) = \frac{\sum_{ns=0}^{NS} a_{ns} \cdot s^{ns}}{\sum_{ds=0}^{DS} b_{ds} \cdot s^{ds}} \tag{2.38}$$

where $s = j \cdot \omega$, ω is the angular frequency in radians per second. *H(s)* can be scattering, admittance, or impedance parameters. The goal of solving Equation 2.38 is to represent the frequency response *H(s)* as a rational function by computing the orders *NS* and *DS* and the coefficients a_{ns} and b_{ds} of the numerator and denominator, respectively [21].

There are many approaches to obtain the coefficients of the above rational function [22]. Choi et al. showed one of the effective procedures to calculate the needed coefficient [23], which is briefly explained as bellows.

Equation 2.38 can be rewritten in the form:

$$\sum_{ns=0}^{NS} a_{ns} \cdot s^{ns} - H(s) \sum_{ds=0}^{DS} b_{ds} \cdot s^{ds} = 0 \tag{2.39}$$

As *H(s)* is the measured data or simulated data, Equation 2.39 can be written as a matrix equation:

$$[A]\begin{bmatrix} a \\ b \end{bmatrix} = [0] \tag{2.40}$$

By multiplying the transpose of [A], Equation 2.40 becomes:

$$[A]^T [A][x] = [0] \tag{2.41}$$

By [22, 24], the above equation can be written as:

$$[A]^T [A][x] = \lambda_{\min}[x] \tag{2.42}$$

where λ_{min} is the minimum eigenvalue of the matrix. Choi, et al. solved Equation 2.42 using the eigenvalue method. To solve the equation, the estimation of the integer orders, *NS* and *DS*, should be preceded. After determining the orders, the eigenvector [*x*] related to the minimum eigenvalue λ_{min} can be computed. The stability should be enforced using the root finding method [25]. The matrix [A] in Equation 2.52 can be reformulated to compute the residues corresponding to the stable, common, real and complex conjugate poles as below:

$$\begin{bmatrix}
\mathrm{Re}\left\{\sum_m \frac{1}{(s_1 - p_m)} \;\; \sum_n \frac{2(s_1 - p_{nr})}{(s_1 - p_{nr})^2 + p_{ni}^{\;2}} \;\; \sum_n \frac{-2p_{ni}}{(s_1 - p_{nr})^2 + p_{ni}} \;\; \sum_k \frac{s_1}{(s_1 - p_k)} \;\; 1 \;\; 0 \;\; -G(s_1)\right\} \\
\mathrm{Im}\left\{\sum_m \frac{1}{(s_1 - p_m)} \;\; \sum_n \frac{2(s_1 - p_{nr})}{(s_1 - p_{nr})^2 + p_{ni}^{\;2}} \;\; \sum_n \frac{-2p_{ni}}{(s_1 - p_{nr})^2 + p_{ni}} \;\; \sum_k \frac{s_1}{(s_1 - p_k)} \;\; 0 \;\; s_1 \;\; -G(s_1)\right\} \\
\vdots \\
\mathrm{Re}\left\{\sum_m \frac{1}{(s_1 - p_m)} \;\; \sum_n \frac{2(s_1 - p_{nr})}{(s_1 - p_{nr})^2 + p_{ni}^{\;2}} \;\; \sum_n \frac{-2p_{ni}}{(s_1 - p_{nr})^2 + p_{ni}} \;\; \sum_k \frac{s_1}{(s_1 - p_k)} \;\; 1 \;\; 0 \;\; -G(s_1)\right\} \\
\mathrm{Im}\left\{\sum_m \frac{1}{(s_1 - p_m)} \;\; \sum_n \frac{2(s_1 - p_{nr})}{(s_1 - p_{nr})^2 + p_{ni}^{\;2}} \;\; \sum_n \frac{-2p_{ni}}{(s_1 - p_{nr})^2 + p_{ni}} \;\; \sum_k \frac{s_1}{(s_1 - p_k)} \;\; 0 \;\; s_1 \;\; -G(s_1)\right\}
\end{bmatrix}
\begin{bmatrix} \gamma_1 \\ \vdots \\ \alpha_1 \\ \vdots \\ \beta_1 \\ \vdots \\ \varphi_1 \\ \vdots \\ \delta \\ \eta \\ 1 \end{bmatrix}
=
\begin{bmatrix} 0 \\ 0 \\ \vdots \\ \vdots \\ 0 \\ 0 \end{bmatrix} \tag{2.43}$$

Equation 2.43 includes the real residues γ_m for real poles p_m, complex conjugate residues $\alpha_n \pm j\beta_n$ for complex conjugate poles $p_{nr} \pm jp_{ni}$, real residues φ_k for real poles p_k, and it has a constant residue δ, linear frequency dependent residue η, and the frequency response G. The real parts and imaginary parts are separated to ensure that the coefficients of rational functions are real.

Since the solution using the eigenvalue method can generate inaccurate poles, vector fitting was proposed to extract accurate stable poles of the rational function [26]. The fundamental formulation for vector fitting using the pole-residue form of the rational function can be written as:

$$\left(\sum_{ds=1}^{DS}\frac{r_{ds}}{s-p_{ds}}+d+e\cdot s\right)=\left(\sum_{ds=1}^{DS}\frac{R_{ds}}{s-p_{ds}}\right)\cdot H(s) \tag{2.44}$$

Using the given poles p_{ds} of the rational function, the residues r_{ds} and R_{ds} values should be calculated. A constant residue d or a linear frequency dependent residue e may be included on some applications. After estimating the order DS and the stable poles p_{ds} of the rational function, the method computes the residues using the least square approximation, as shown in Equation 2.43. For extracting new poles in the next step from the residues R_{ds}, Equation 2.56 can be transformed as:

$$H(s)=e\cdot\frac{\sum_{ds=1}^{DS+1}(s-z_{ds})}{\sum_{ds=1}^{DS}(s-Z_{ds})} \tag{2.45}$$

where the zeros z_{ds} and Z_{ds} are the zeroes of the rational function in the left and right side of Equation 2.44, respectively, and Z_{ds} are used in the following step. The unstable poles

of Z_{ds} are appropriately modified for satisfying the stability condition in the iteration process. If the initial guess of the poles is appropriate, the vector fitting method generates accurate poles and residues.

When it comes to multi-port system macromodeling, it is more difficult to solve the corresponding matrix equation. A linear time-invariant system with a N-port network can be represented as:

$$[H(s)] = \begin{bmatrix} H_{11}(s) & H_{12}(s) & \cdots & H_{1N}(s) \\ H_{21}(s) & H_{22}(s) & \cdots & H_{2N}(s) \\ \vdots & \vdots & \ddots & \vdots \\ H_{N1}(s) & H_{N2}(s) & \cdots & H_{NN}(s) \end{bmatrix} \tag{2.46}$$

If the system has common poles, Equation 2.46 can be rewritten as:

$$[H(s)] = \frac{[Q(s)]}{P(s)} = \frac{\begin{bmatrix} Q_{11}(s) & Q_{11}(s) & \cdots & Q_{1N}(s) \\ Q_{21}(s) & Q_{21}(s) & \cdots & Q_{2N}(s) \\ \vdots & \vdots & \ddots & \vdots \\ Q_{N1}(s) & Q_{N1}(s) & \cdots & Q_{NN}(s) \end{bmatrix}}{P(s)} \tag{2.47}$$

When the system is symmetric ($H_{ij}(s) = H_{ji}(s)$) along with the common pole assumption, Equation 2.46 can be written in the matrix equation form as:

$$\begin{bmatrix} A_1 \\ \vdots \\ A_m \\ \vdots \\ A_M \end{bmatrix} [x] = [0] \;\Leftrightarrow\; [A][x] = [0] \;\Leftrightarrow\; [A]^T[A][x] = \lambda_{\min}[x] \tag{2.48}$$

where M is the number of frequency samples. Equation 2.48 can be solved by the eigenvalue method.

Rational function is easily implemented into the commercial circuit simulation tools. For example, one of the prevalent circuit simulators, *Spice*, provides several function calls such as *Laplace Transform* or *Pole-zero Function*. However, the procedure for finding appropriate coefficients of the rational function is not an easy task. As you read in this section, there have been many approaches to handle this problem efficiently, but each method has some strengths and some weaknesses.

The frequently pointed out problems of the macromodeling approach are summarized as bellows. First, macromodeling needs a special calculation technique; it requires effective algorithm to generate a reasonable set of coefficients for the rational function, and it demands software-coding procedure implementing considerable matrix manipulation and computation. As that kind of knowledge and skill is available for the limited specialists, general engineers have no choice but to use an available commercial macromodel providing software tool such as *Broadband Spice*®. But the lumped element equivalent circuit model we propose does not need a special software program for implementation, it only needs general optimization function that is easily found in circuit simulators like *Spice* or *ADS*®. Second, macromodel undergoes the problem of unstable poles. This causes the most troublesome issue in the computer aided circuit simulation, convergence error. Even commercial tools cannot avoid this intrinsic problem of the macromodeling. However, the lumped passive element equivalent models are free from this trouble, because they inherently satisfy the passivity conditions: 1) all poles of [*H(s)*] are placed on the left half of the *s*-plane, 2) [*H(s)*] does not have multiple poles on the imaginary axis of he *s*-plane, 3) the eigenvalues of *Re*[*H(s)*] are positive or zero for all frequencies,

and 4) the coefficients of [*H(s)*] are all real. Third, macromodel cannot deliver internal information of the equivalent model. This originates from the fact that this method represents only input-output relationship with numerical expression; it does not include physical meaning on each coefficient of the model. On the contrary, the lumped element model we propose in the dissertation can provide some useful information of the device from the viewpoint of circuit design. It directly shows parasitic components such as a bonding wire or substrate capacitance, or it can give us a rough 3 dB bandwidth by the component values in the resonant circuit parts.

Chapter 3 An Improved Wideband Laser Diode Model

3.1 Motivation

As discussed in Chapter 2, rate equation-based laser diode models require too many device parameters such as optical confinement factor, carrier density at transparency, photon lifetime, spontaneous emission factor, carrier lifetime, volume of the active region, etc. [27]. From the point of a circuit design engineer, measuring all these parameters is practically impossible, because a broad and deep understanding of the laser diode physics, long measure time, and accurate facilities to take the measurements are necessary. Then, even if all the parameters are measured, if the actual devices show some non-ideal behavior or if the measured material properties differ from the material properties of the fabricated device, then the resulting model will not be accurate.

Finite-difference time-domain (FDTD) method can provide a more rigorous analysis of the physical phenomenon inside a laser diode, taking into account non-ideal geometric effects on the device behavior: however, this method consumes enormous computer CPU time, and only if the material properties of the lasers are known very well, it will provide an accurate simulation result. Although FDTD simulation could be the best choice for laser diode manufacturing engineers who have full access to material properties, this method is not an attractive approach for circuit design engineers.

This research proposes to overcome the problems of conventional laser diode models by introducing a fast and accurate measurement-based modeling approach. A wide-band lumped element circuit model is for commercial discrete laser diode modeling, and a scalable equivalent circuit model is for the laser diode that allows physical dimension scaling. The former is covered in Chapter 3.2, and the latter is delivered in Chapter 3.3.

A small number of attempts reported in literature [28-31] showed relatively promising results by a rate equation model or a heuristic circuit model, but these models were not scalable, thus it is impossible for circuit designers to change the dimensional parameters of the laser by using the models. If they have an effective scalable laser diode equivalent model, they can generate accurate results in less time using fewer resources.

To verify the validity of this proposed method, we fabricated several printed-circuit-boards (PCBs) for 622 Mbit/s and 2.5 Gbit/s commercial multiple quantum well laser diodes, and showed the device performance is well predicted by the model. For the scalable laser model, we used several different cavity length laser devices from the group of Prof. Nan Jokerst to make a scalable laser diode model. The measurement results and simulation results are discussed in detail in this chapter.

3.2 The Proposed Wideband Lumped Element Laser Diode Model

To compare the new method to existing heuristic modeling approaches, a very accurate high frequency equivalent circuit laser model will be developed. This model is more advanced when compared with current models of similar type reported in the literature [31].

3.2.1 Equivalent Circuit Model for Commercial Lasers

A multiple resonance small-signal equivalent circuit model for commercial Fabry-Perot semiconductor lasers is presented to express both input reflection and electrical-to-optical transmission over a wide-frequency range. Its effectiveness is demonstrated by comparing measured and simulated eye-diagrams. An example of a direct-modulated laser drive circuit design demonstrates the accuracy of the proposed model. This model can improve laser drive circuit performance by the enabling proper design of the matching circuit.

3.2.1.1 Test Preparations for Commercial Lasers

We purchased and tested two kinds of connectorized commercial laser diodes at the operating speeds of 622 Mbit/s and 2.5 Gbit/s. The reason for selecting the laser diode operating speeds less than 4 Gbit/s or 5 Gbit/s is that it is almost impossible at those speeds to de-embed the effects of parasitics of the low speed commercial printed circuit boards such as a fiberglass resin (i.e., FR-4) with calibration standards using ultra-small surface mount packages and microstrip elements [32, 33]. The features of the chosen

1310 nm Fabry-Perot laser diodes modules are summarized in Table 3.1, and their optical and electrical characteristics are presented in Table 3.2.

Table 3.1 The selected commercial laser diode features.

Characteristics	622 Mbit/s Laser	2.5 Gbit/s Laser
Structure	Multi quantum well	Multi quantum well
Wavelength	1310 nm	1310 nm
Laser Diode Type	Fabry-Perot	Fabry-Perot
Operating Temperature	-40 °C to +85 °C Uncooled	-40 °C to +85 °C Uncooled
Packaging	FC receptacle with 2-hole flange	FC receptacle with 2-hole flange
Applications	SONET OC-3/OC-12	SONET OC-3/OC-48

Table 3.2 The selected commercial laser diode optical and electrical characteristics at 25 °C.

Characteristics	622 Mbit/s Laser	2.5 Gbit/s Laser
Threshold Current	12 mA (typ.)	10 mA (typ.)
Fiber Output Power	0.6 mW (min) @I_{op} =32mA	1 mW (typ.) @ I_{op}=25mA
Peak Wavelength	1280/1310/1340 nm	1290/1310/1330 nm
Spectrum Width	2 nm (typ.)	3 nm (max.)
Forward Voltage	1.2 (typ.)	1.2 (typ.)
Rise Time/Fall Time	0.7 ns (max.)	150 ps (max.)
PD Monitor Current	0.1 mA (min.)	100 μA (min.)
PD Monitor Dark Current	100 nA (max.)	0.1 μA (max.)
PD Monitor Capacitance	8 pF (typ.)	6 pF (typ.)

Table 3.3 summarizes the maximum ratings. One of the important consideration factors in test board production is soldering temperature. Excessive soldering-induced thermal stress can degrade the performance of a laser diode; meaning temperature stress could lower the light output power level and/or slow down the maximum operating speed. Paying careful attention to soldering time should avoid similar destructive effects from excessive temperature.

Table 3.3 The selected laser diode maximum ratings at 25 °C.

Characteristics	622 Mbit/s Laser	2.5 Gbit/s Laser
Laser Forward Voltage	1.2 V	1.2 V
Laser Reverse Voltage	2 V	2V
Soldering Temperature	< 260 °C	< 260 °C
Soldering Time	< 10 sec	< 10 sec

The printed circuit board layout and the implemented board for the selected 622 Mbit/s laser diode are presented in Figures 3.1 and 3.2, respectively. The physical distances from SMA connectors to the through-hole positions of the laser diode anode and cathode are controlled as short as possible to reduce the parasitic effects of printed circuit board. As the built-in InGaAs photodiode is solely for monitoring average light output power level, the long electrical length of the strip line between the photodiode anode and the corresponding SMA connector does not affect the system performance. In this sense, a longer path length is assigned to the photodiode SMA connector. The purpose of the right side rectangular block, as shown in Figure 3.1, is to measure the effect of the laser diode strip line path. Given that the actual operating frequency at the data speed of 622

Mbit/s is less than 500 MHz, the angle change between laser diodes input ports is designed to have less than 10° difference; thus, it is possible to disregard the effect of strip lines and SMA connectors.

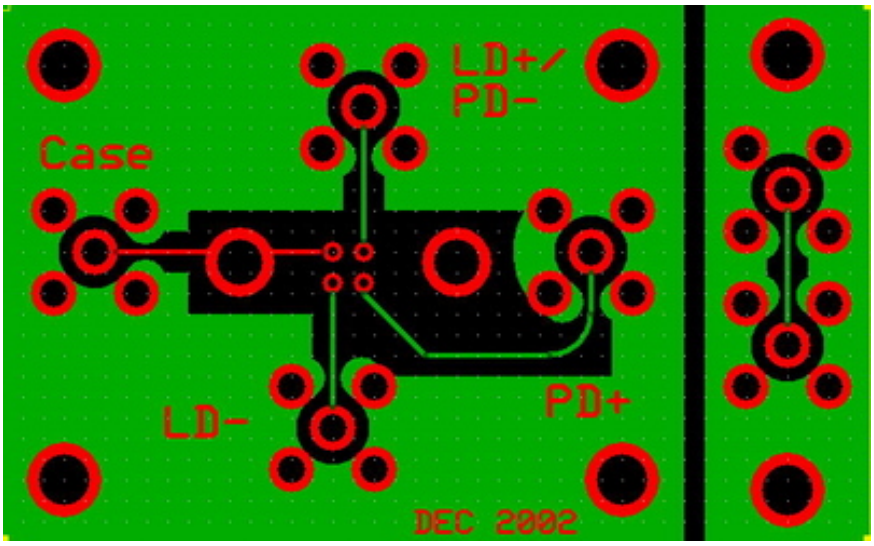

Figure 3.1 The printed circuit board layout for the selected 622 Mbit/s laser diode.

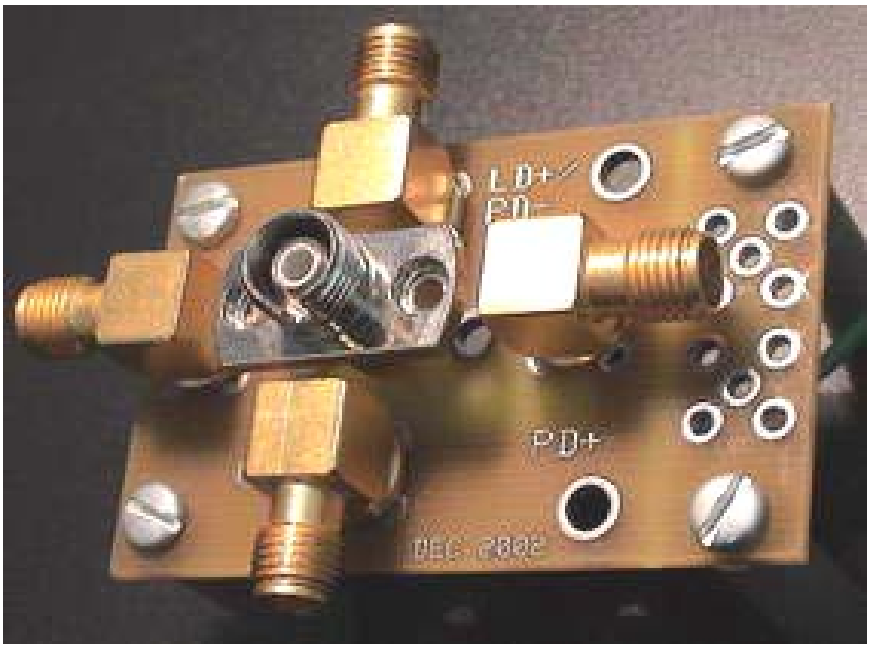

Figure 3.2 The fabricated 622 Mbit/s laser diode mounted on the printed circuit board.

Special considerations should be given to de-embed the effects of strip lines and SMA connectors in the 2.5 Gbit/s laser diode printed circuit board design. The printed circuit board layout and the fabricated test board with the 2.5 Gbit/s connectorized laser diode are presented in Figures 3.3 and 3.4, respectively. As operating speed increases over 1.0 GHz, electrical wavelength shrinks to the order of several centimeters; thus, distributed models must be used for simulation to include the parasitic effects, such as signal transmission loss, propagation delay, and dispersion.

The short-open-load (SOL) calibration kit, one of the simplest calibration structures, is implemented on the circuit board where the laser diode is positioned. Short structure is realized by a via-hole from the laser diode anode pad to the ground, or by several wire connections between the laser pad and the ground. No special setup is applied to facilitate an open structure; a simple air open is used under the condition of sustaining the same physical distances from the surrounding components. Since the physical size of the applied surface mount chip resistor becomes comparable to the quarter wavelength of the given operating speed, introducing an accurate 50 Ω load structure is the most difficult part at the stage of calibration kit implementation. To reduce unwanted parasitic effects, the 0.04 inch long and 0.02 inch wide ultra small 402 series surface mount technology resistor is utilized, as shown at the right bottom edge of Figure 3.3. The through hole line in the middle of the board divides the board into two separate boards, which reduces the printed circuit board fabrication cost. Several dummy patterns are also included in the board to deal with various situations; for example, 50 Ω load pad using two parallel 100 Ω resistors is added to have a more precise 50 Ω load resistor.

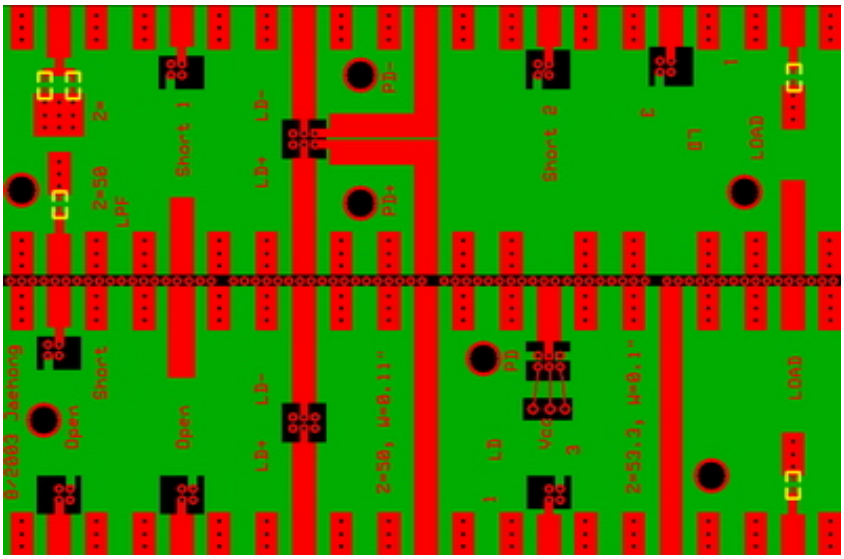

Figure 3.3 **The printed circuit board layout for the selected 2.5 Gbit/s laser diode,**

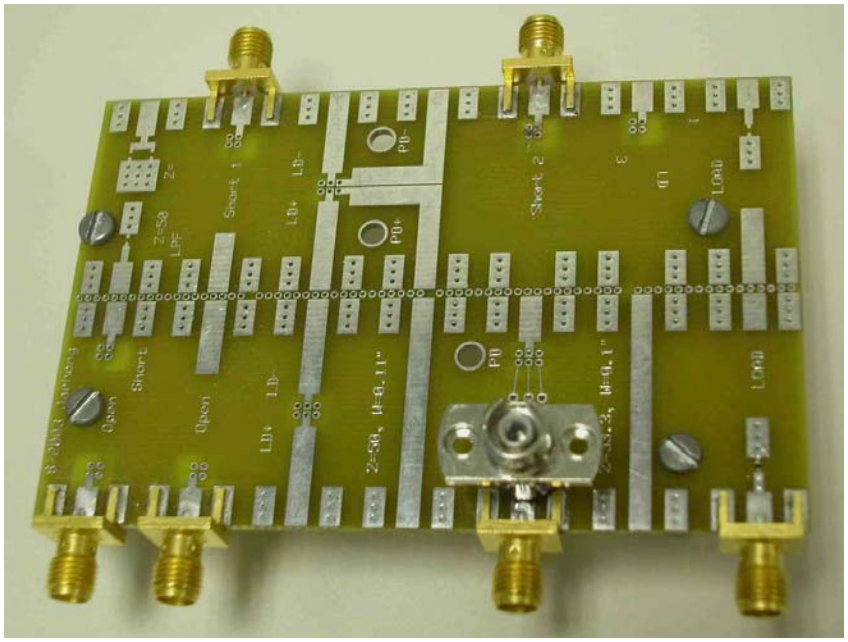

Figure 3.4 **The fabricated 2.5 Gbit/s laser diode mounted on the printed circuit board.**

3.2.1.2 Measurement Results

Before conducting AC measurements of the selected laser diodes, DC performance should be evaluated to select an appropriate operating bias point that ensures reasonable light output power. A common DC test, named an L-I-V sweep test, constitutes the foundation of all laser diode characterization. The nomination arises because the test measures optical light output (L), input driving current (I), and induced diode voltage (V). An L-I-V curve includes forward voltage measurements on the laser diode, a lasing threshold current test, and optical light output power measurement. Figure 3.5 shows the 622 Mbit/s laser diode L-I-V performance.

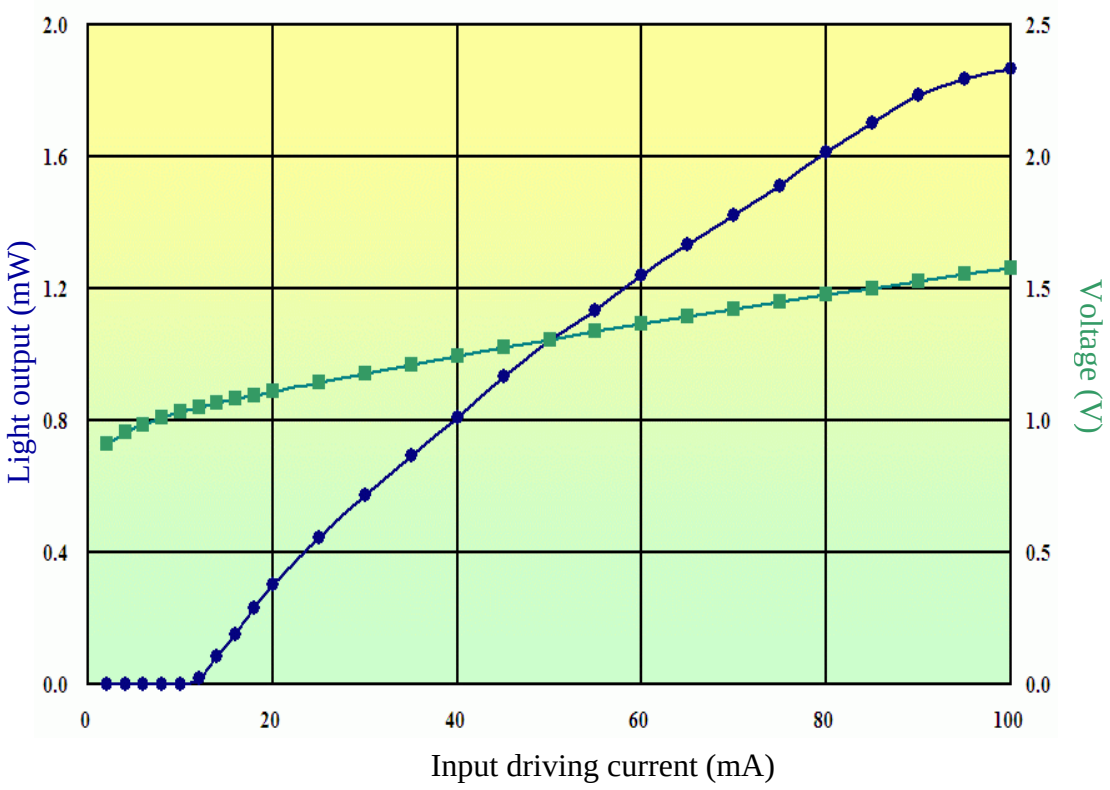

Figure 3.5 The L-I-V sweep test result for the 622 Mbit/s laser diode.

As mentioned in the electrical specification sheet (Table 3.2), the optical output power level indicates 0.6 mW at 30 mA driving current and the threshold current level records 12 mA.

Similarly, Figure 3.6 shows the L-I-V sweep test result for the selected Fabry-Perot 2.5 Gbit/s laser diode. This device shows better performance than the given electrical specification in Table 3.2. Additionally, 8 mA threshold current and 1.18 mW light output power at 25 mA current driving are demonstrated in the actual measurement.

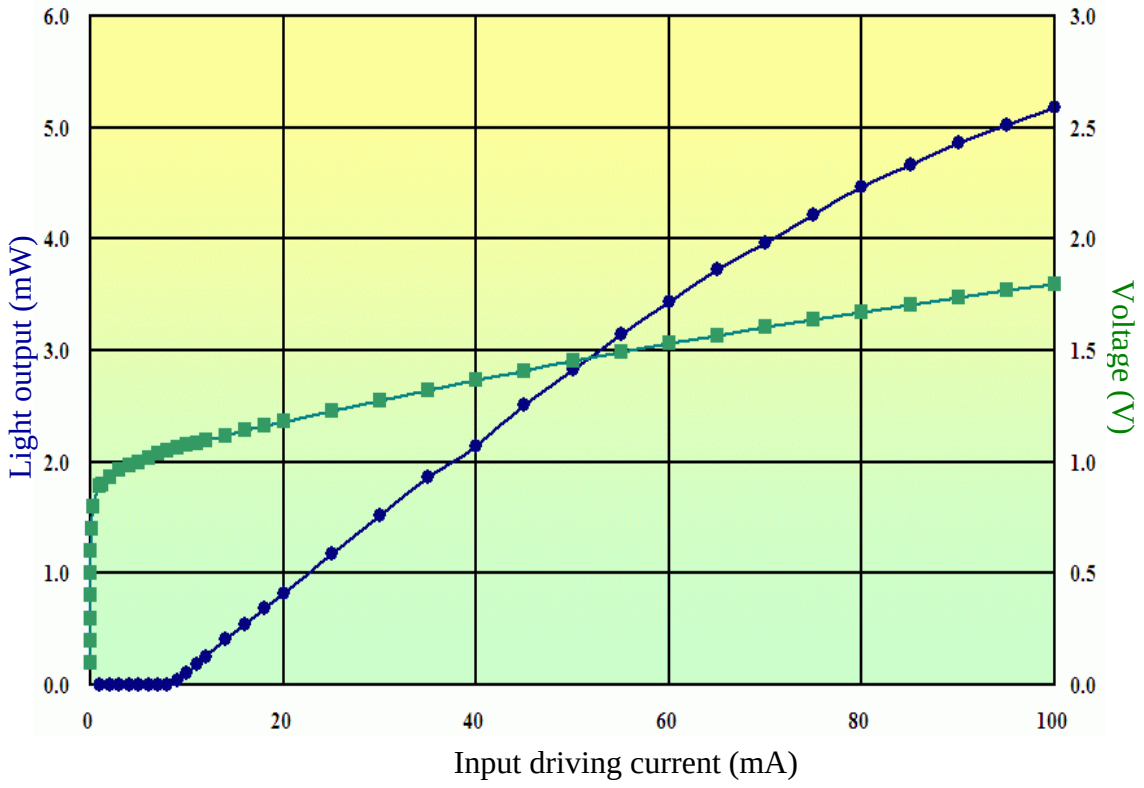

Figure 3.6 The L-I-V sweep test result for the 2.5 Gbit/s laser diode.

The measured input return loss response of the commercial 622 Mbit/s 1310 nm Fabry-Perot laser diode module is presented in Figure 3.7. As shown, multiple resonances occur in the high frequency region where laser driving input signal could have appreciable spectral components in the real-world situation; thus, an appropriate model should be developed to express these effects up to the high frequency band. Because 1.55 GHz frequency is the fifth harmonic of the 622 Mbps square wave, the laser diode model covering up to the 1.6 GHz frequency band can be named as a wideband model.

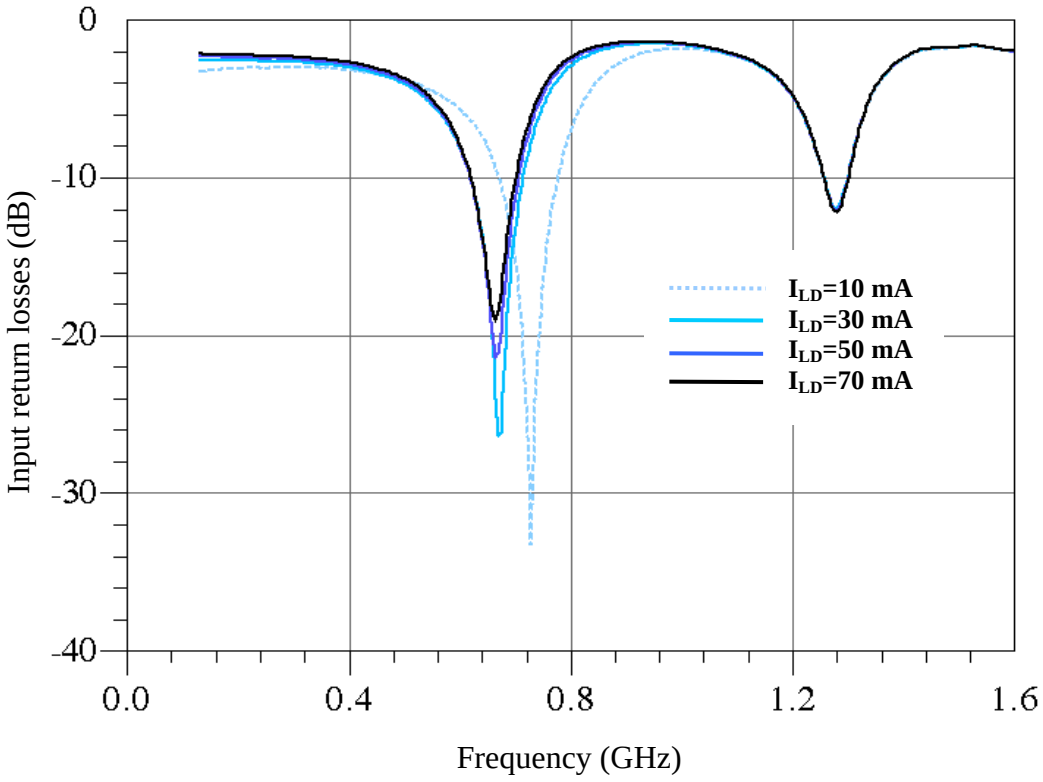

Figure 3.7 The measured input return loss responses of the 622 Mbit/s laser diode.

The input return loss responses in Figure 3.7 suggest that those responses over the threshold current level (i.e., 12 mA in the 622 Mbit/s laser diode) have stable performances.

We therefore consider that this laser diode is linear in the higher bias current points than the threshold current level; thus, it is possible to make a small signal model with lumped elements only.

Figure 3.8 shows the input return loss responses in the Smith chart format, which is a powerful tool for designers to develop their intuition about transmission line and impedance matching problems. When a given device possesses a complicated trajectory on Smith chart like the response in Figure 3.8, the model needs more passive components to express the complex responses in the linear modeling.

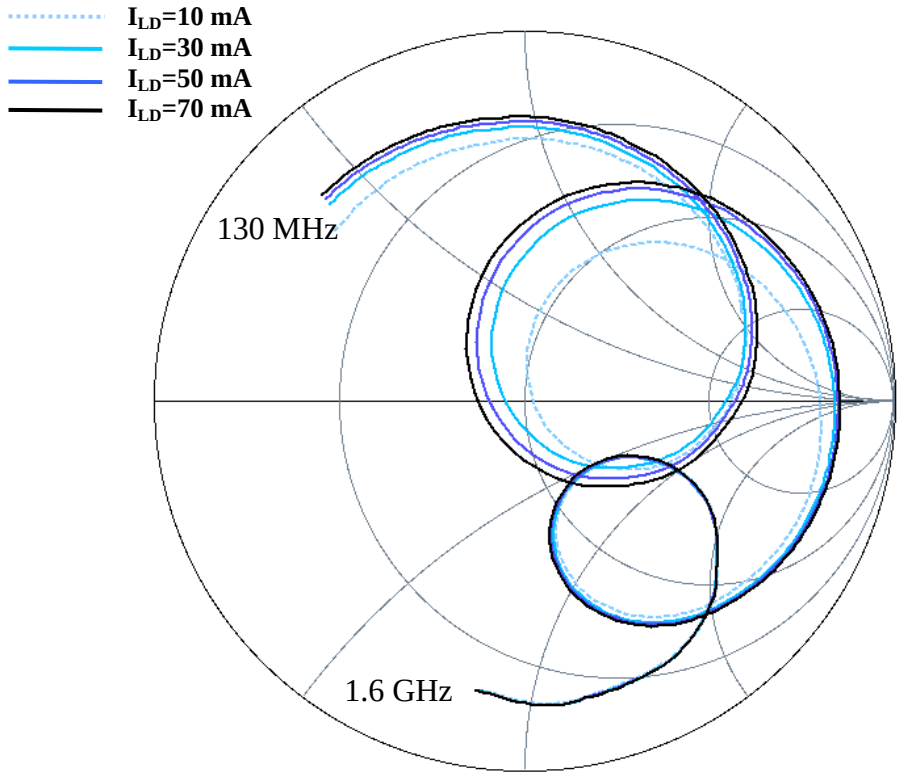

Figure 3.8 The measured input return loss responses of the 622 Mbit/s laser diode on the Smith chart.

The measured electrical-to-optical transfer responses of the selected 622 Mbit/s Fabry-Perot laser diode are presented in Figure 3.9. Those responses also show that the responses over the threshold current level are stable, that is, they differ very little along bias points, while the response under the threshold current level has a big deviation from the rests.

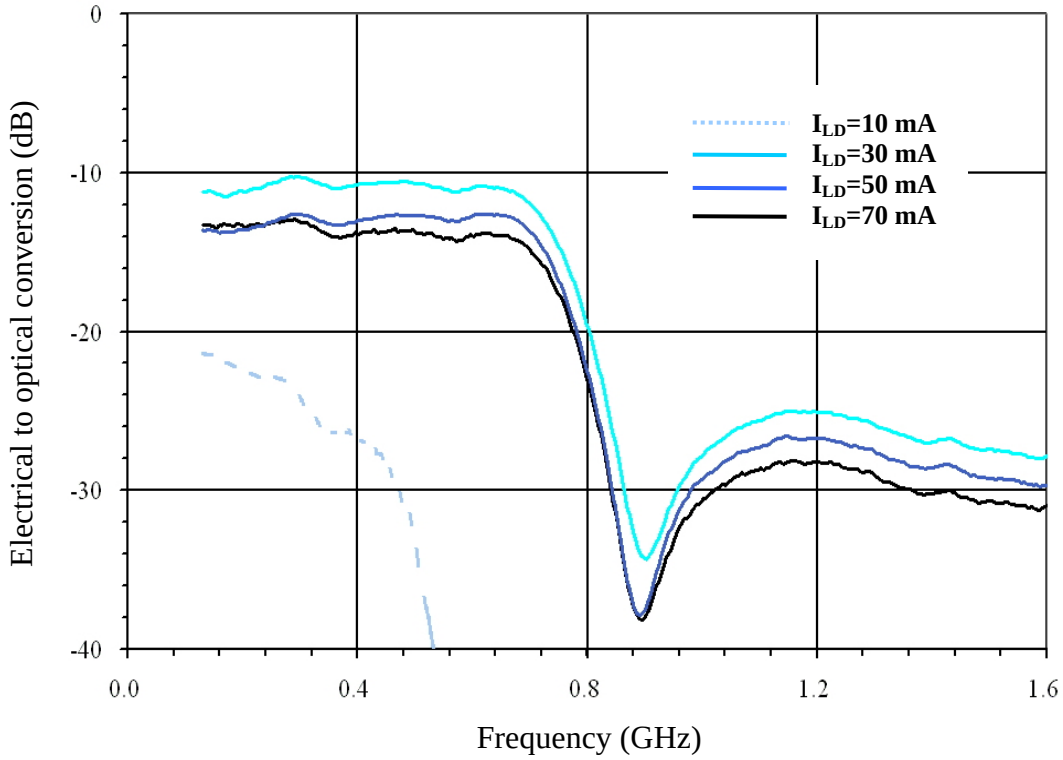

Figure 3.9 The measured electrical-to-optical conversion responses of the 622 Mbit/s laser diode at several different bias points.

The measured input return loss response and the electrical-to-optical conversion response of the 2.5 Gbit/s laser diode at 30 mA current bias point are presented in Figures 3.10 and 3.11, respectively. The input return loss response has simpler trajectory than that of the 622 Mbit/s laser diode responses.

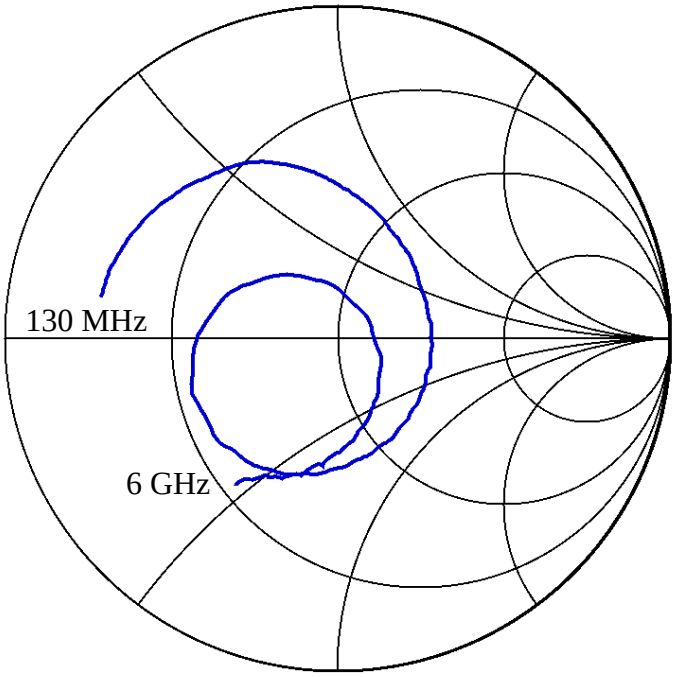

Figure 3.10 **The measured input return loss response of the 2.5 Gbit/s laser diode on the Smith chart.**

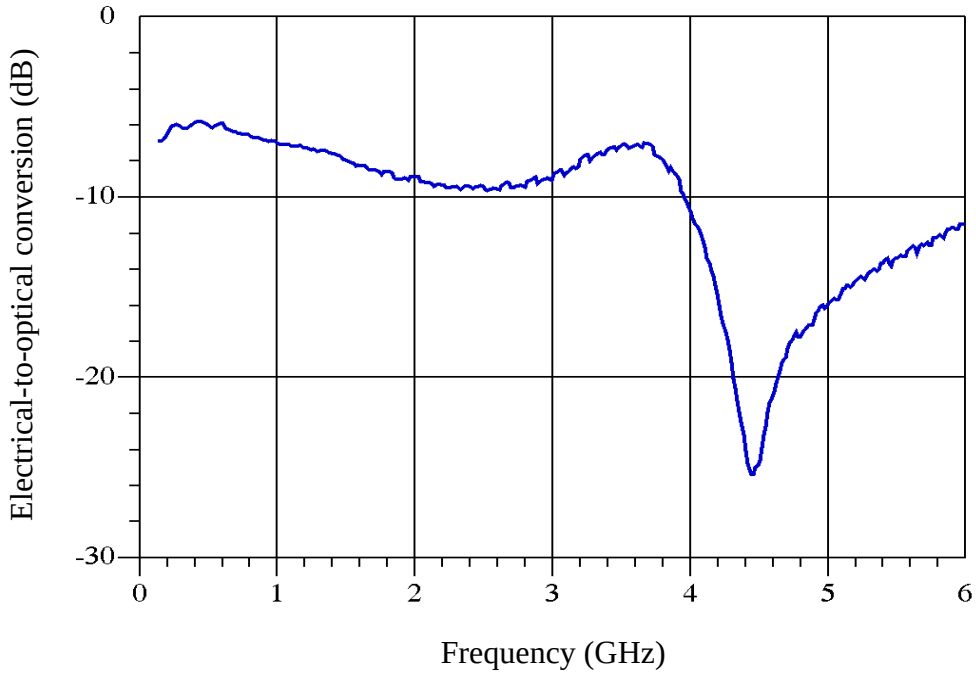

Figure 3.11 **The measured electrical-to-optical conversion response of the 2.5 Gbit/s laser diode.**

3.2.1.3 Multiple Resonance Lumped Element Model

The simplest single mode laser diode model can be presented by a single resonant circuit with parallel conductance, capacitance, and inductance components as shown in Figure 3.12. The energy stored in the cavity determines the inductance and the capacitance values, L and C, respectively. The gains and losses in the laser diode decide the conductance value, G [30].

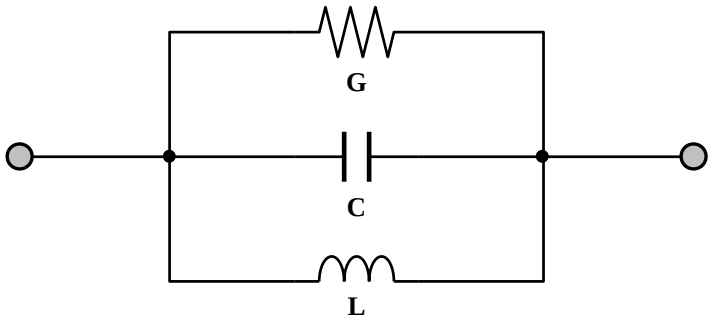

Figure 3.12 The simplest single mode laser diode equivalent circuit model.

To build an enhanced model for the laser diode, a multiple-resonance conductance-capacitance-inductance circuit model [31] is applied to represent both input return loss response and electrical-to-optical transfer response over a wide frequency range. Figure 3.13 displays the proposed multiple-resonance model.

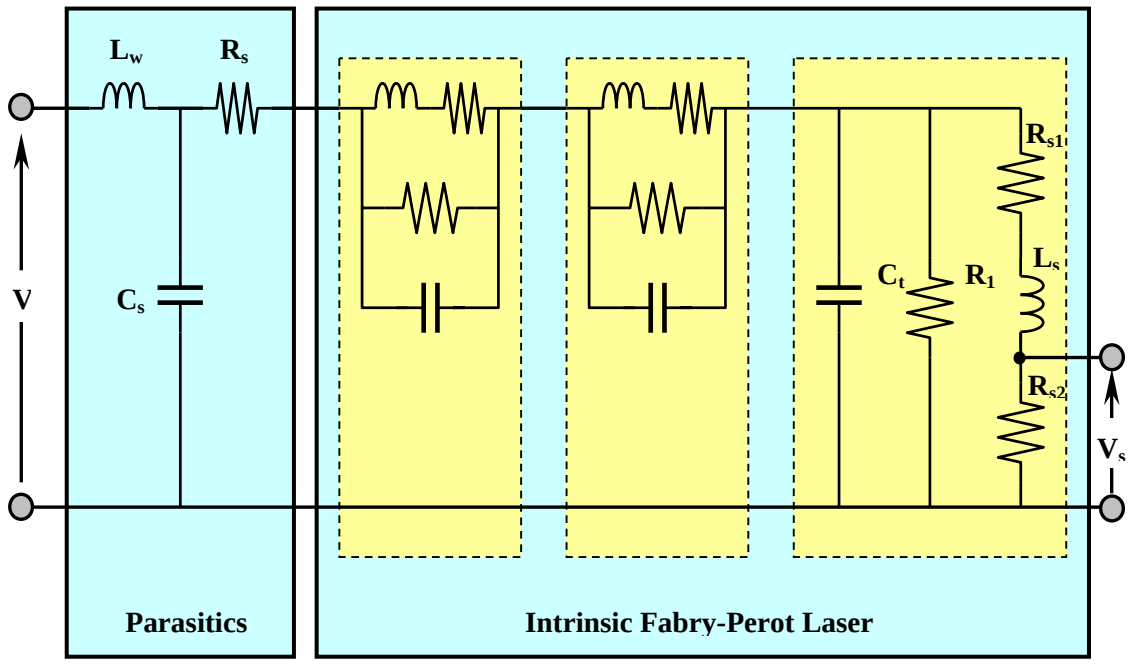

Figure 3.13 Multiple-resonance small-signal lumped element model for Fabry-Perot laser diodes.

The parasitic components include contact capacitance C_s, series resistance R_s between contacts, and bonding wire inductance L_w. In the intrinsic laser model, the small-signal photon storage and the space charge plus active-layer diffusion capacitance are modeled by L_s and C_t, respectively. The other equivalent circuit parameters, R_{s1}, R_{s2}, and R_1 are related to the laser diode electrical direct-current (DC) characteristics. Lastly, the output voltage across R_{s2} represents the optical intensity of a laser [31]. To establish the model parameters bounds are determined for each parameter to maintain physical meaning, and then the equivalent circuit element values are extracted by fitting the frequency responses of the proposed small-signal lumped element model with the scattering parameter sets measured from a light-wave component analyzer.

The comparison of the measured input return loss response and the model calculated response is shown in Figure 3.14. A good agreement is observed over a high frequency range.

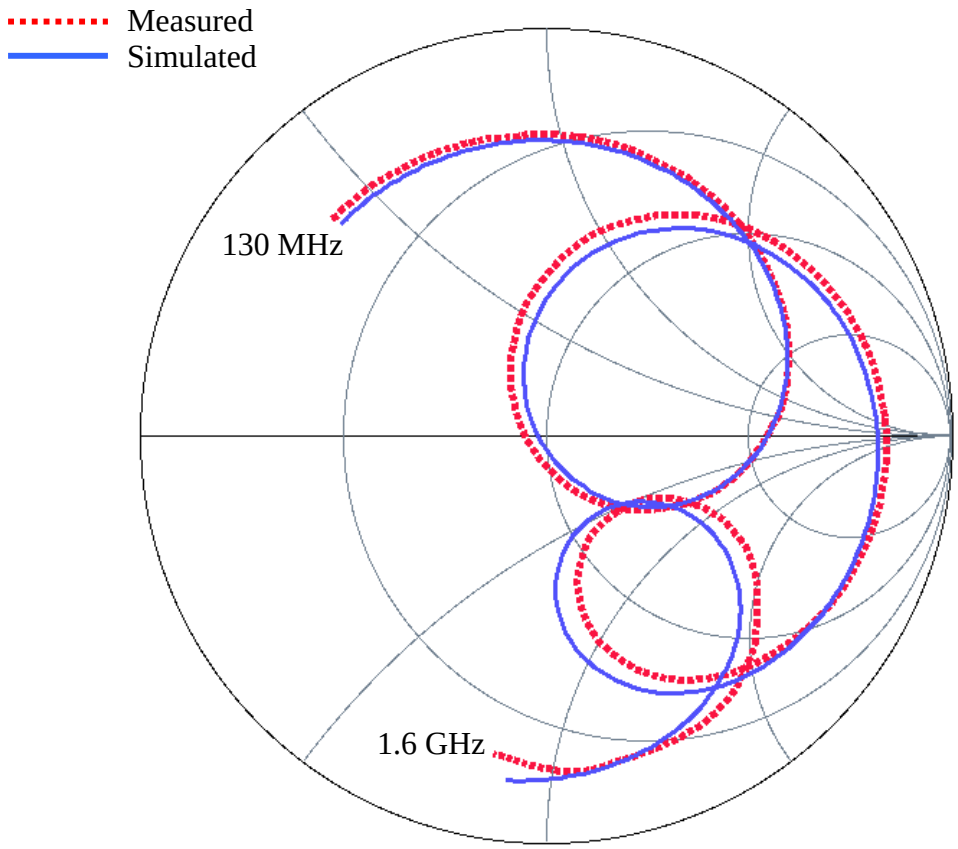

Figure 3.14 Comparison with the calculated input return loss and the measured data.

The model parameters for the electrical-to-optical response should be optimized with the measured data while they maintain the input return loss characteristics. The achieved electrical-to-optical transmission from the equivalent model in Figure 3.15 coincides with the measured data up to 1.2 GHz. These results would have been impossible to implement with a conventional single resonance model.

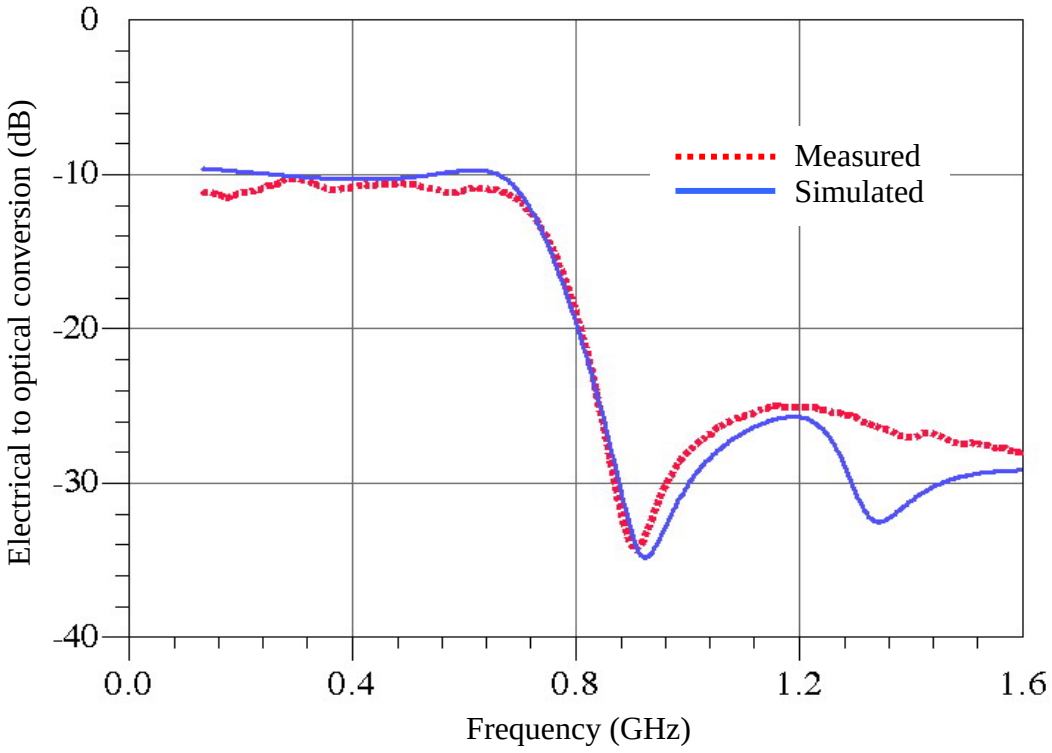

Figure 3.15 Comparison with calculated electrical-to-optical transfer response and measured data.

3.2.1.4 Eye-Diagram Simulation

An eye-diagram is a simple and strong visual method to evaluate a digital transmission system. By measuring the width of an eye opening both in the horizontal direction and in the vertical direction, the information about a system's inter-symbol interference (ISI), noise and jitter is obtained.

The measured eye-diagram for a commercial 622 Mbit/s Fabry-Perot edge-emitting laser is shown in Figure 3.16. The signal was detected using a 10 Gbit/s photo-detector having a flat response up to 8 GHz; thus, it is possible that the effect of including the photo-detector into the total measurement system is negligible.

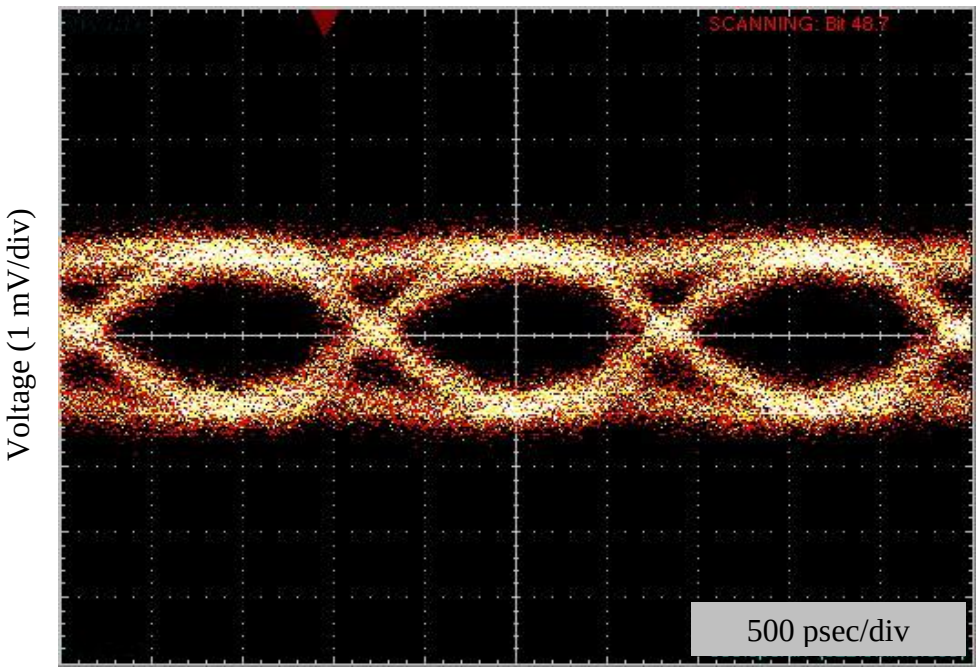

Figure 3.16 **The measured eye-diagram from a commercial laser connected with a photo-detector at 622 Mbit/s.**

A simulated transient analysis using the equivalent circuit model was performed to simulate the eye-diagram of the laser diode. In Figure 3.17, the result obtained from the equivalent model simulation shows almost similar characteristics with the measured data in Figure 3.16. The overall data transition response is well predicted.

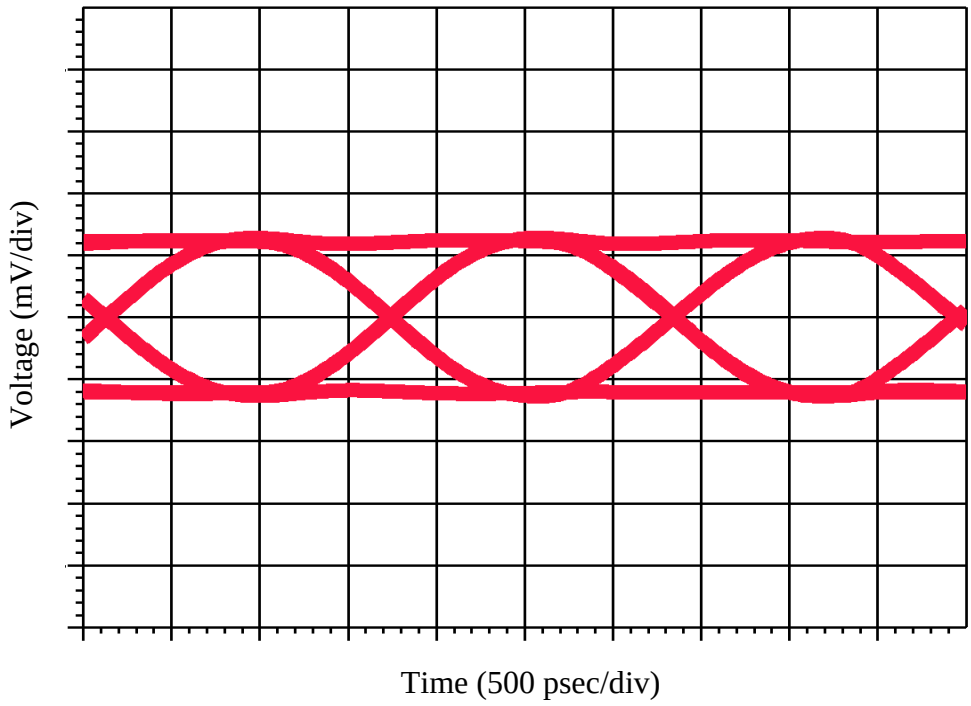

Figure 3.17 The simulated eye-diagram using the proposed model at 622 Mbit/s.

3.2.1.5 The Proposed Model Application for a Laser Driver Circuit Design

The main application area of a semiconductor laser diode model is an optical transmitter circuit design. Several types of laser driver circuits have been developed with various technologies in terms of the different application areas [32-33]. A single-ended type laser drive circuit and a differential type laser drive circuit are presented in Figure 3.18.

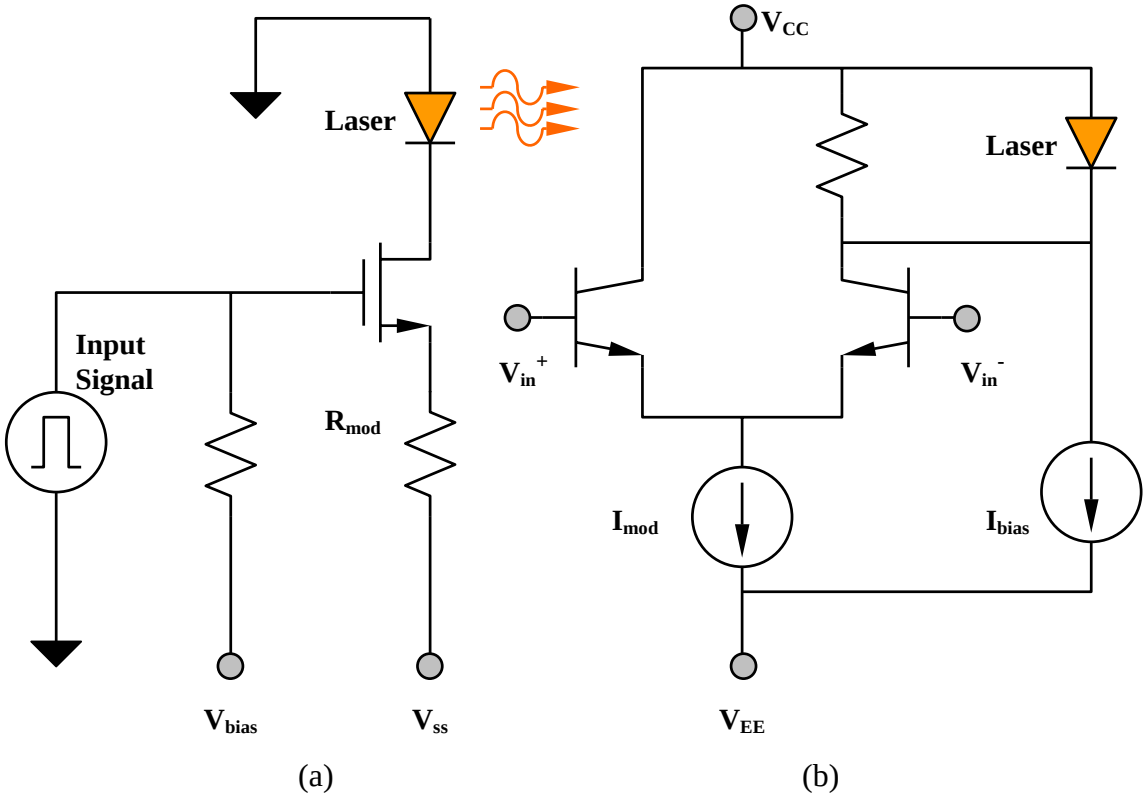

Figure 3.18 (a) Single-ended laser drive circuit, and (b) differential type laser drive circuit.

A laser diode model has been assumed to be a simple resistor in the conventional laser drive circuit. In this case, the frequency-limited characteristics of a real laser cannot be considered at the stage of circuit simulation, which severely degrade circuit performance prediction. The simulations on a single-ended laser drive circuit are performed with a

resistor load and with the proposed laser model at data rates of 622 Mbit/s and 1 Gbit/s to examine the effects of the model.

The applied transistor from Taiwan Semiconductor Manufacturing Company (TSMC) 0.18μm CMOS process does not impose any speed-limitations in this frequency range. A simple resistor-type laser diode model does not predict the system performance degradation at high operating frequency (Figure 3.19). However, the simulation results using the proposed model successfully present more accurate and reliable responses of the real-world circuit design situation (Figure 3.20).

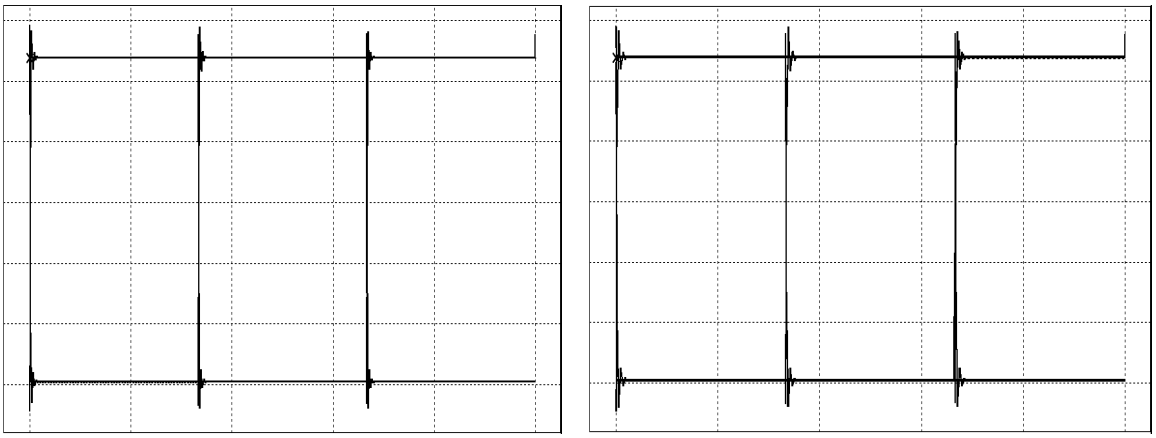

(a) (b)

Figure 3.19 Eye-diagram simulation results using a simple resistor model at 622 Mbit/s (a), and at 1.0 Gbit/s (b),

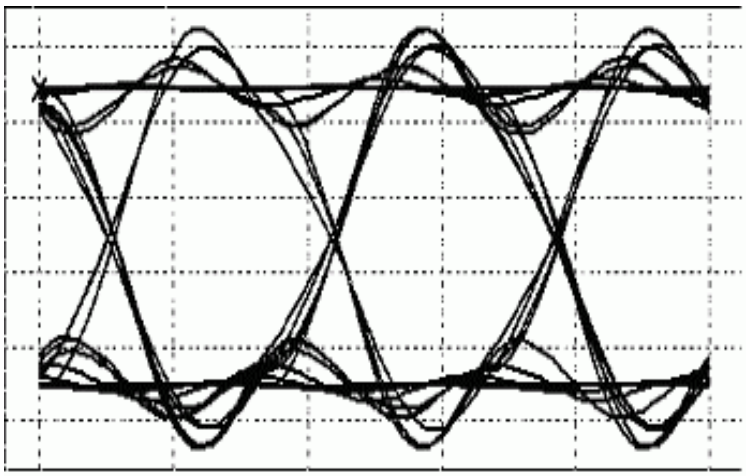

(a)

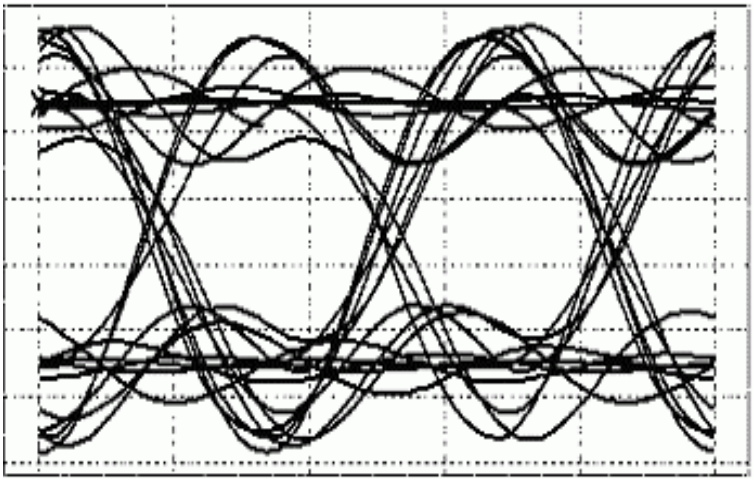

(b)

Figure 3.20 Eye-diagram simulation results using the proposed model at 622 Mbit/s (a), and at 1.0 Gbit/s (b).

3.3 The Proposed Scalable Laser Diode Modeling

Previously, a building block-based modeling methodology was demonstrated as effective in the scaleable modeling of microwave passive devices [34, 35]. The fundamental idea behind the modeling procedure is that most designed structures can be split into fundamental geometrical building blocks that a designer could clip together to make a wide variety of useful devices. Although these building blocks can be defined in a number of ways, careful selection results in only a few building blocks being needed. If accurate models for each of the building blocks along with interaction information can be obtained, then any arbitrary structure comprised of those building blocks can be modeled accurately using the individual block models.

3.3.1 An Example using the Building Block-Based Modeling Methodology

Figure 3.21 shows the building block modeling of a meander resistor test structure is shown in. The serpentine geometry of the resistor can be divided by four fundamental building blocks: 1) A probe pad to connect to the test equipment; 2) A square building block with connections on opposite sides; 3) A U-shaped section connecting two parrarel segments of the resistor; and 4) A coupled block segment to characterize line-to-line coupling behavior on a per-square basis.

Each building block is modeled as a resistor-inductor-capacitor (RLC) circuit (Figure 3.22). The total de-embedding elements is 22 and the number of building blocks is 4.

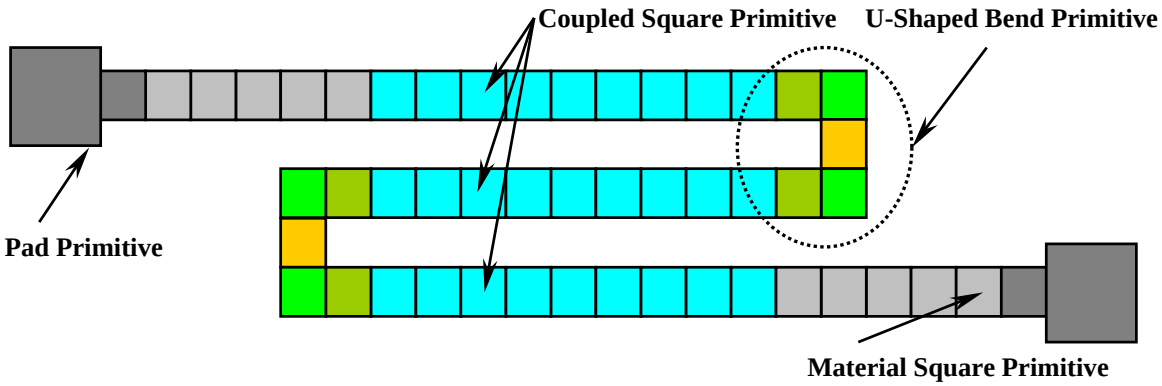

Figure 3.21 A three-segment meander resistor for building block-based modeling.

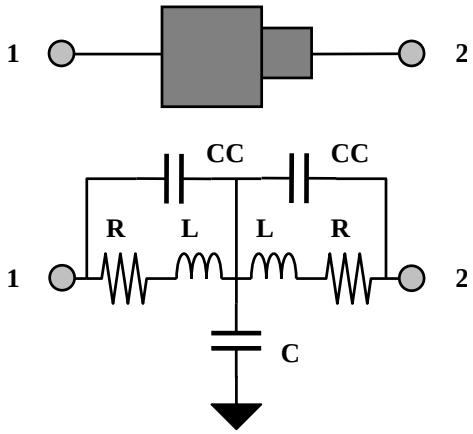

Figure 3.22(a) Building block-based equivalent circuit model for the pad primitive part.

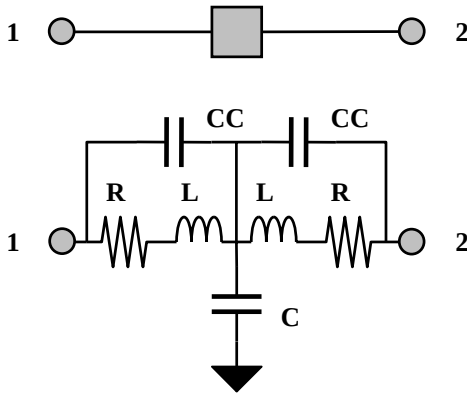

Figure 3.22(b) Building block-based equivalent circuit model for the material square primitive part.

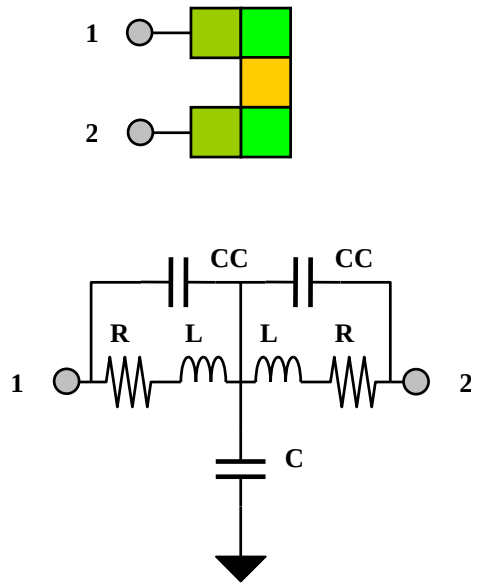

Figure 3.22(c) Building block-based equivalent circuit model for the U-shaped band primitive part,

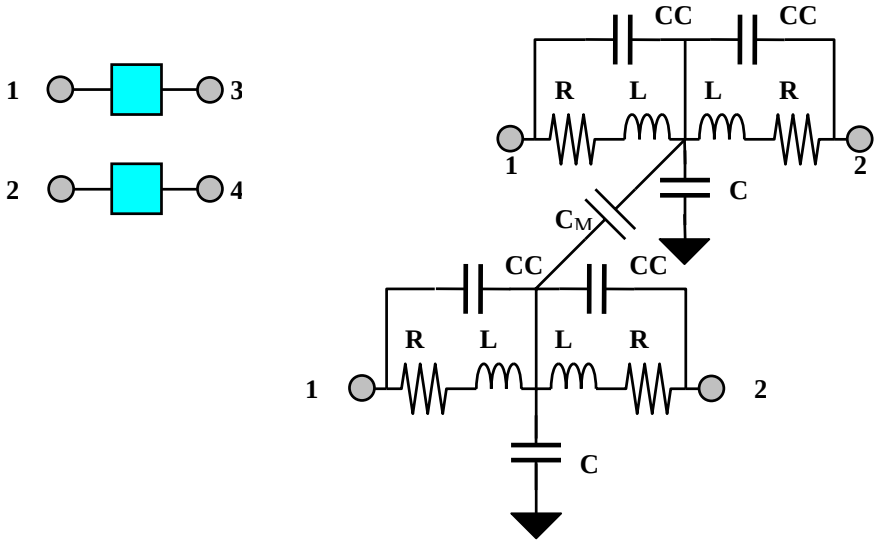

Figure 3.22(d) Building block-based equivalent circuit model for the coupled square primitive part.

When test structure fabrication and building block circuit extraction are completed, the measured scattering parameter data is then used to determine initial guesses and to set up optimizations to extract equivalent circuits of the test structure and building blocks. Using Hspice or ADS optimization tool, the de-embedded circuit values of the building block equivalent circuits are obtained. The circuit designer now has an accurate Spice-level model of each building block, which can then be used to design any value or configuration meander resistor. In previous work [36], the behavior of a nine-segment meander resistor was predicted from the three-segment meander resistor model using the building block-based model.

Although a laser diode is an active device, it is assumed to be a linear device in the small operating region. Particularly, a laser diode shows quite linear performance beyond the threshold current level. For this reason, the building block-based modeling methodology can be applied to laser modeling.

3.3.2 Building Block-Based Scalable Laser Diode Modeling

In general, the physical parameters of a laser diode have not been used for optimizing the performance of an opto-electronic circuit design. On the contrary, conventional electrical active devices, such as CMOS, bipolar, and hetero-junction bipolar transistors, provide various sizing choices for the optimization of overall circuit performance. Several changeable parameters comprise laser diode fabrication, including cavity length, ridge width, and mirror reflectivity. If material level control is possible, band-gap engineering through changing the number of quantum wells, doping concentration, or introducing strained layers will allow more flexibility in a design. From a practical point of view, cavity length change is perhaps the best parameter to vary as it can be easily achieved with device cleaving, and it results in significant changes in output power and frequency response.

The concept of scaling laser diode cavity length is presented in Figure 3.23. Changing cavity length can be expressed with changing the number of basic cells in the middle region.

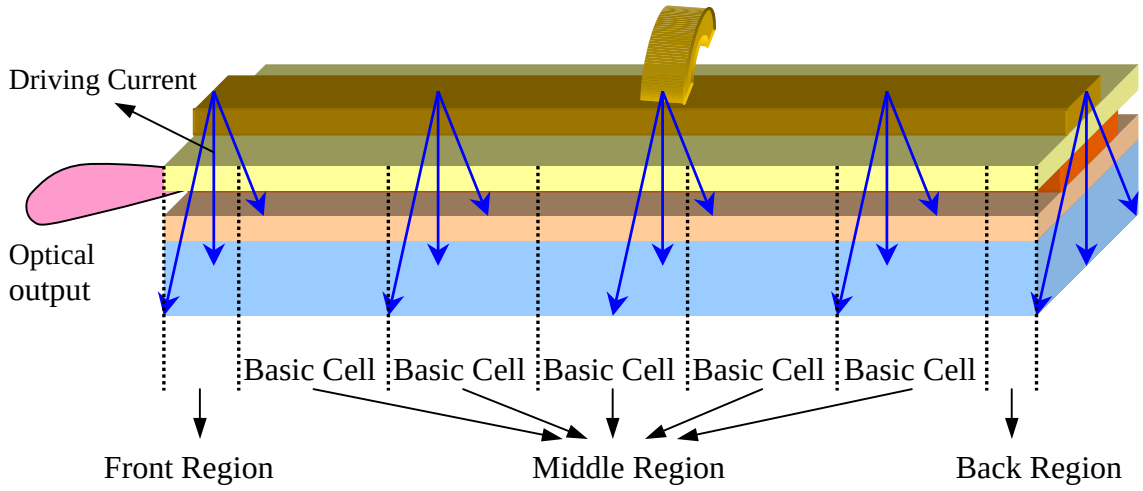

Figure 3.23 **Conceptually divided regions for a scalable laser diode model.**

The laser front region and back region are considered separately to represent the different conditions at the cavity edges. For example, the anti-reflection coated backside plane of a cavity could be differently modeled than any other block such as front block or basic block. Figure 3.24 depicts a possible building block-based, cavity length scalable, small-signal high-frequency equivalent circuit model.

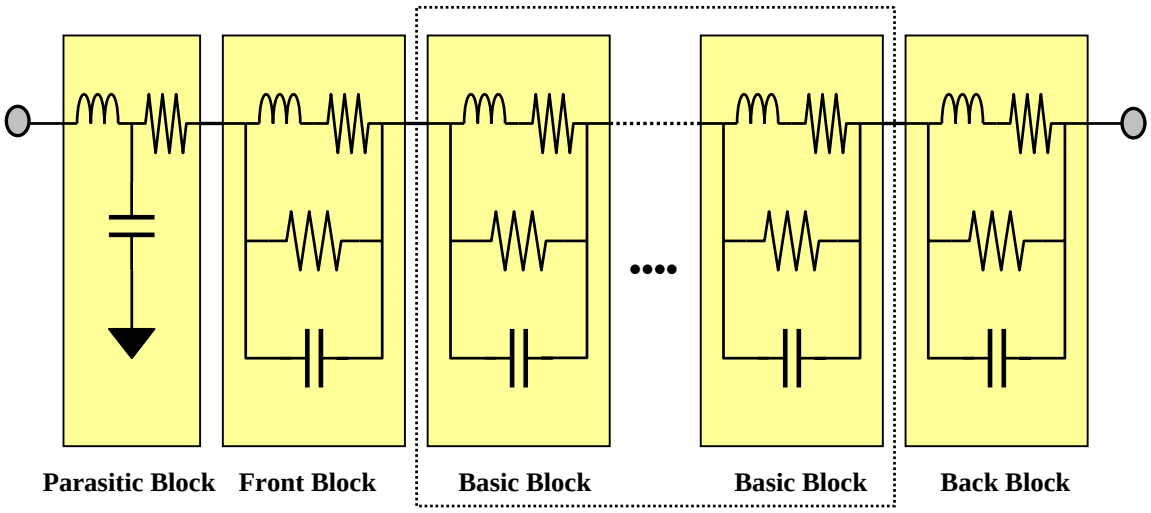

Figure 3.24 **Building block-based, cavity length scalable, small-signal high-frequency equivalent circuit model for edge emitting laser diodes.**

The goal of this research is to develop and validate this type of scalable laser diode model. Parasitic components such as contact capacitance, contact series resistance, and bonding wire inductance, are modeled in the parasitic block. The dots in the middle region present the repetition of the basic blocks. The effect of DC bias on the linear components will also be addressed. This will most likely take the form of a series of models at different bias current per block. The possibility of developing a scalable unified large-signal model will be investigated but may be beyond the scope of this current project.

In summary, laser diode cavity length variation or ridge width variation can provide different electrical properties in a circuit design, which expands the flexibility of performance optimization. Scalable equivalent circuit models for those devices enable circuit designers to simulate accurate performance before actual fabrication.

3.3.3 Ridge Waveguide Laser Diode Fabrication and Measurement

3.3.3.1 Multiple Quantum Well Laser Diode Fabrication

1.3 μm wavelength InP/InGaAsP 5 quantum well ridge waveguide (RWG) lasers are implemented at the Microelectronic Research Center (MiRC) by Prof. Nan M. Jokerst's group.

Before proceeding into DC and high-frequency measurement sections, a brief review of the fabricated laser diode physical structure is given. The top view of the lasers is given in Figure 3.25 (a), and a three-dimensional schematic representation is shown in Figure 3.25 (b). A microwave probe is used to measure the performance of the devices (left side of Figure 3.25 (a)). The common microwave probe is a ground-signal-ground (GSG) type, but a signal-ground (SG) or ground-signal (GS) type probe is also adopted in case a narrow pitch size probe is required. As the cavities of the lasers are obtained by cleaving, the cavity lengths remain the same. The individual ridge widths are different, as indicated in Figure 3.25 (a).

The side view of the laser structure in Figure 3.25 (b) shows about a 2 μm height difference between the p-type anode pad and n-type cathode pad. Benzocyclobutene (BCB) based polymer dielectric material is deposited on the laser surface, and then via holes make connections to each pad. Using this method, both anode and cathode pads can be made on the same level. This planar pad design is specifically developed to avoid probe contact problems during microwave measurements.

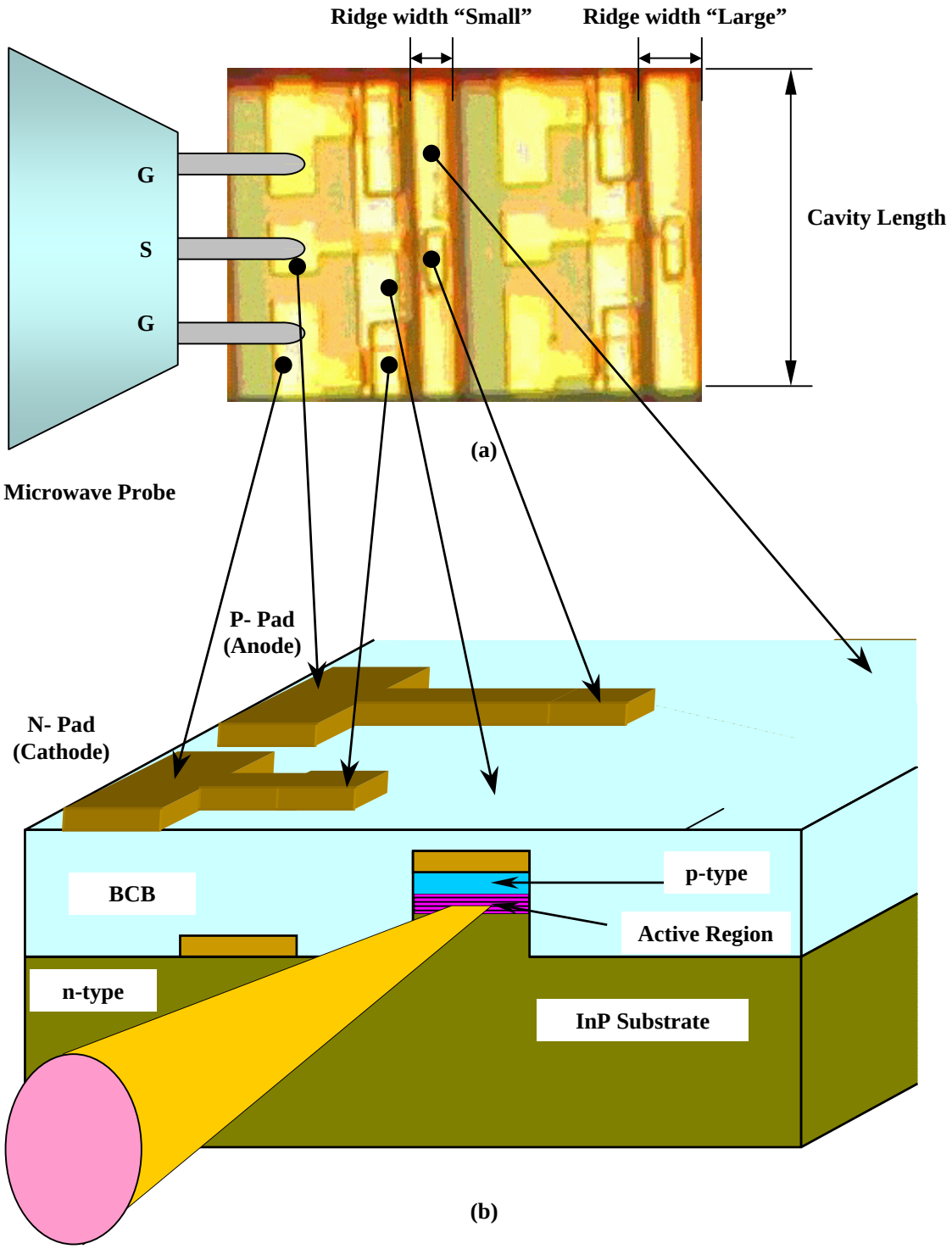

Figure 3.25 The fabricated 1.3 μm multiple quantum well ridge waveguide edge-emitting laser diodes picture and three dimensional schematic representation of the device. (Courtesy of Sangwoo Seo)

3.3.3.2 Measurement

3.3.3.2.1 DC Performance Measurement

The nonlinear DC light-current (L-I) relationship of a laser is important from the circuit design standpoint. A laser diode having a high threshold current level needs high DC bias current, which increases overall power dissipation in the system. The circuit designer needs to ensure that the input current dynamic range is positioned above the threshold current level to ensure high-speed operation.

The light-current (L-I) characteristics of the fabricated 1.3 μm wavelength multiple quantum well edge-emitting thin-film laser diode were measured (Figure 3.26).

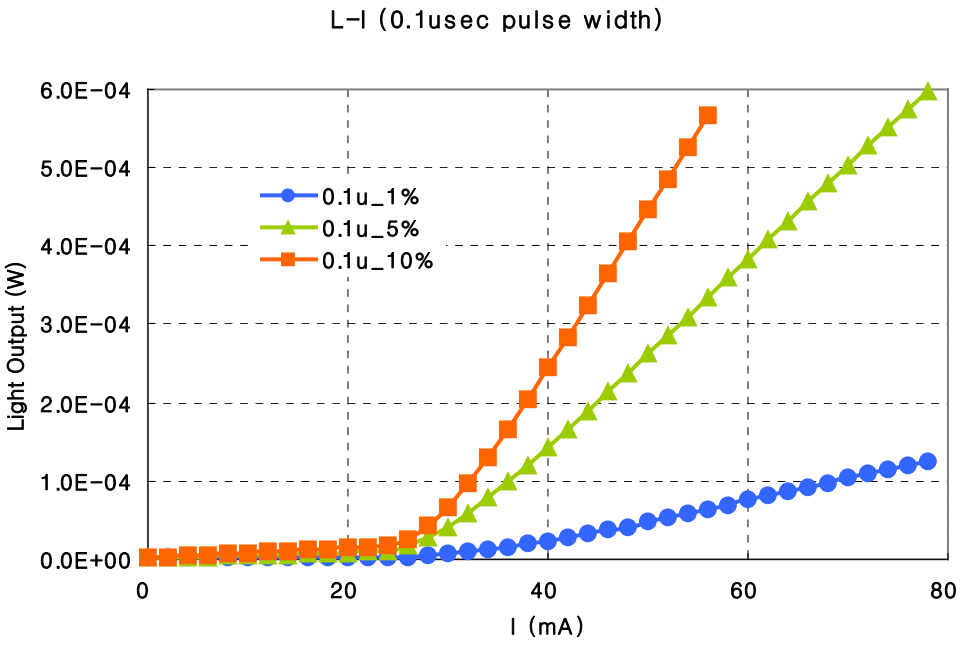

Figure 3.26 The average light-current characteristics of the fabricated thin-film laser diode at 0.1 μsec pulse duration and with different duty factors. For increased duty factor there is more light as the laser is on for more time.

The measured laser showed a 28 mA threshold current and 0.02 mW/mA slope efficiency. When the pulse duration is fixed, an increased duty factor – i.e., increased driving current causes the laser diode to generate more light output. Unfortunately, the fabricated thin-film laser could not be operated continuously at room temperature (continuous wave or CW operation), which is an unexpected drawback. As seen in Figures 3.26 and 3.27, the light output for short pulse lengths (0.1 and 0.3 μsec) at 10 % duty factor shows clear laser operation.

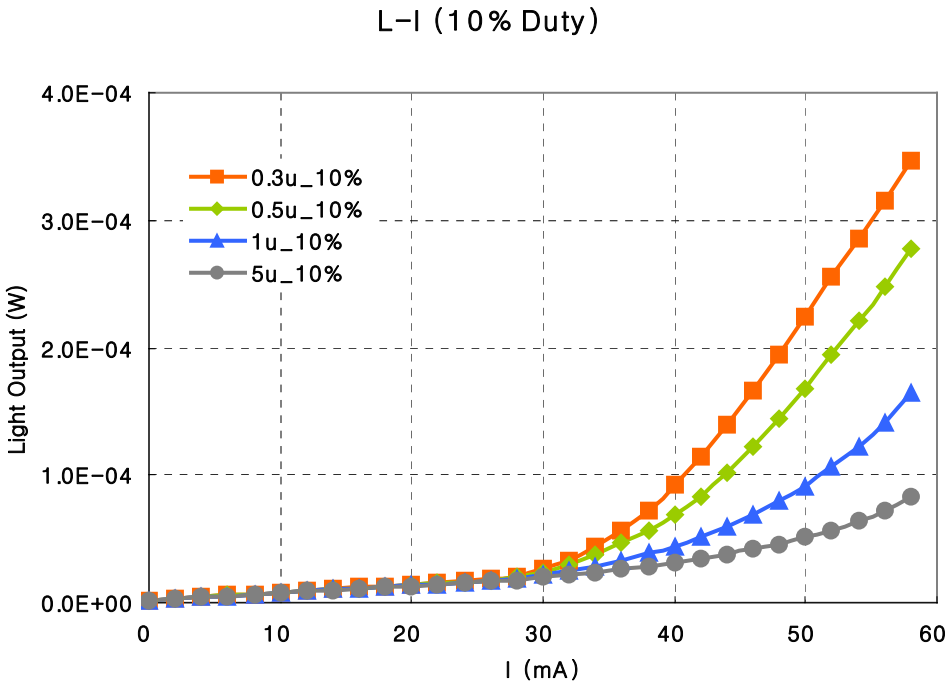

Figure 3.27 Light-current (L-I) characteristics of the fabricated thin-film laser diode at different pulse durations with the 10 % duty factor.

However, as shown in Figure 3.27, longer pulse lengths cause the laser to stop lasing. As our focus lies on finding a reliable scalable laser diode modeling, we used numerically derived scalable rate equation model to show the validity of the proposed scalable laser diode model.

3.3.3.2.2 Laser Diode Calibration for High Frequency Measurement

A laser diode is an electro-optic device converting an electrical input signal into an optical output signal. Thus, both electrical input reflection characteristics and electrical-to-optical (E/O) transfer characteristics should be considered in the equivalent circuit model. The two other factors normally required for complete scattering parameters, namely, optical-to-electrical feedback and optical output reflection, will be assumed to be negligible for circuit design applications.

Whenever we measure the characteristics of a laser diode, several unwanted and inevitable errors are included in the measurement data. Thus, calibration is needed to de-embed those errors. Typical errors are non-ideal input power source, cables, on-wafer probe, and signal detector. Figure 3.28 shows an example of a custom-made calibration kit. After calibration, the measurement reference plane becomes the plane "B," removing the effects of all of interconnects to that point. Conventional RF calibration would only remove the effects of interconnects to the plane "A" in Figure 3.28.

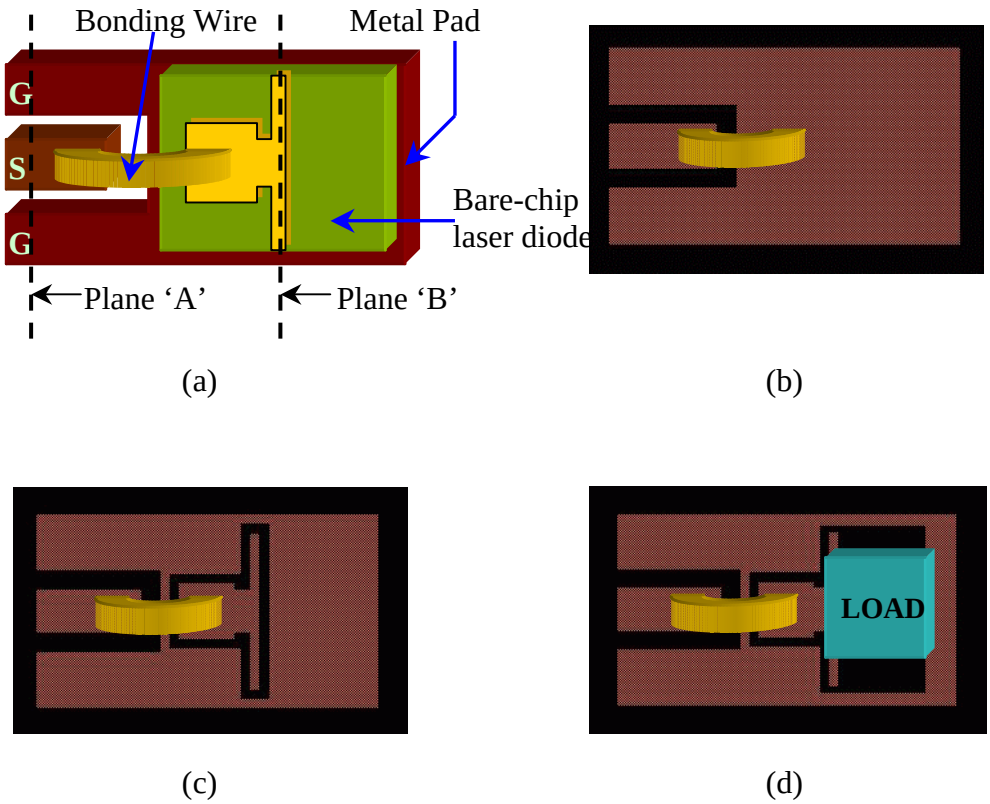

Figure 3.28 (a) Bare-chip laser diode on the pad, (b) short mask, (c) open mask, and (d) load mask.

3.3.3.2.3 Direct Modulation High Frequency Performance Measurement

One of the most important aspects of laser diode operation is its high-frequency response. In other words, when the laser current is directly modulated from a drive circuit, we are interested in how fast the laser diode responds to the input change and whether the light output faithfully follows the given current drive pulse or not.

The electrical-to-optical transfer performances of the fabricated laser diode bare chips were measured with the HP 8703A Lightwave Component Analyzer (LCA). The calibrated internal photo-detector of an LCA transforms optical power of a laser diode into an electrical current form. Characterizing a laser diode with LCA scattering parameter measurement results is the most precise and convenient approach. Unfortunately, as mentioned in the previous section, CW (non-pulsed) operation of the fabricated laser diodes has not been obtained. We considered several possible solutions to this problem. However, none produced reliable measurement. A possibility of making enhanced laser diodes emitting stimulated light output at room temperature has not been rule out. However, laser diode fabrication is beyond the proposed research.

One of the practical solutions was a pulsed mode transient response measurement. Its likelihood was demonstrated in the laser DC performance measurement showing significant stimulated-light emission in a short pulse input. The approach is based on that the modulated input signal with a sine wave and a short pulse train does not make a laser diode enter the region of spontaneous emission operation. When analyzing the output

waveform of a laser, additional consideration should be given to a turn-on time interval of the laser, which degrades laser speed performance because of spontaneous emission.

Shown in Figure 3.29 is a simple schematic of the pulsed mode transient response measurement. If the bandwidth of a photo-detector is wide enough to cover the bandwidth to characterize a laser diode, the calibration of a photo-detector is very easy, because the optical-to-electrical (O/E) transfer performance of a high-speed photo-detector is generally flat.

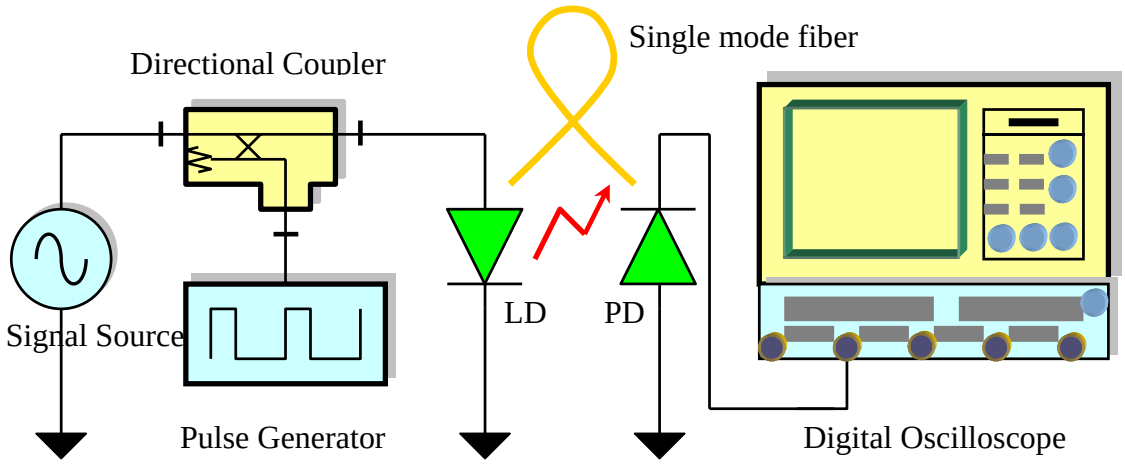

Figure 3.29 The set-up for the pulsed mode transient response measurement.

Before measuring the fabricated quantum well laser diode, we confirmed the validity of this method by testing several commercial laser diodes. However, the measurement results did not show a proper operation.

A more sophisticated measurement was also conducted by using a network analyzer with a pulsed S-parameter configuration that requires a pulse generator to provide the pulse signals and timing to the test set.

3.3.3.3 Conclusion

Despite the extensive trials to measure the fabricated laser diode performance, we could not secure reliable AC measurements. It is considered that the main source of these problems arose from the failure of a stable DC operation. If the fabricated devices were designed with an appropriate thermal consideration, they could have shown reasonable DC and AC performance.

However, the original goal of the latter half of our work is to find and validate a building block-based scalable laser model. Thus, we derived a scalable rate equation model instead of fabricating another quantum well laser diodes. The following chapters explain the prcesses.

3.3.4 Building Block-based Scalable Laser Modeling to the Numerically Derived Scalable Rate Equation

3.3.4.1 Numerical Derivation of the Scalable Rate Equation

One of the laser diode small-signal equivalent circuit models was explained in Chapter 2.3.1. Detailed theoretical derivation and model improvement for device scaling are covered in this section. The modeling components presenting deep-level traps [8] are intentionally omitted and modified to include scalable factors of the quantum well laser diode model.

The single-mode rate equations in Chapter 2.2.1 are modified for convenience of derivation and presented below:

$$\frac{dN}{dt} = \frac{I}{qN_w LWd} - BN^2 - \Gamma G_m C' S \,, \tag{3.1}$$

$$\frac{dS}{dt} = -\frac{S}{\tau_p} + \beta BN^2 + \Gamma G_m C' S \,, \tag{3.2}$$

where C′ is the speed of light in the medium, τ_p is the photon lifetime, β is the spontaneous-emission coupling coefficient, G_m is the optical gain, and B is the conventional band-to-band recombination coefficient. The first equation requires that the time rate of change for the charge density in the active region is equal to the current flow into the region, and carrier losses from spontaneous emission and stimulated emission. In the same manner, the second equation requires that the time rate of change for the photon density in the laser device can be expressed with the absorption in the active region and the sum of spontaneous emission and stimulated emission.

By introducing a new parameter of optical voltage into the equivalent circuit model and applying chain rule, the time rate of change for the charge density can be expressed as

$$\frac{dN}{dt}=\left(\frac{dN}{dV_j}\right)\cdot\left(\frac{dV_j}{dt}\right). \tag{3.3}$$

Equation 3.1 can be written as follows by multiplying qN_wLWd:

$$qN_wLWd\left(\frac{dN}{dV_j}\right)\cdot\left(\frac{dV_j}{dt}\right)=I-qN_wLWd\cdot BN^2-qN_wLWd\cdot\Gamma G_mC'S. \tag{3.4}$$

The active region length and width are given L and W, respectively. The left term on the above equation includes the charge storage effect in the active region.

$$C_n\equiv qN_wLWd\cdot\frac{dN}{dV_j}. \tag{3.5}$$

The radiative recombination current I in the quantum well region, can be presented by rearranging Equation 3.1.

$$I=qN_wLWd\cdot BN^2+\frac{4qL\Gamma G_mP_{out}}{E_{ph}}+C_n\cdot\frac{dV_j}{dt}. \tag{3.6}$$

The average light output power P_{out} that carries the physical information [42], is expressed as

$$P_{out}\equiv(N_wWd)\cdot gL\cdot\frac{E_{ph}C'}{4}\cdot S. \tag{3.7}$$

Then the average light output power emission from the front facet is given as

$$P_{avg}\equiv\frac{(N_wWd)E_{ph}C'}{4}\cdot S. \tag{3.8}$$

where $E_{ph}=\hbar\cdot\omega=h\cdot\nu$.

Using the introduced parameter P_{avg}, the time rate of change for the photon density *dS/dt* can be substituted into the below equation:

$$\frac{dS}{dt} \equiv \frac{4}{(N_w W d) E_{ph} C'} \cdot \frac{dP_{avg}}{dt} . \tag{3.9}$$

Now, Equation 3.2 can be transformed as follow by substituting those above equations:

$$\frac{4}{C'} \cdot \frac{dP_{avg}}{dt} = (N_w W d E_{ph}) \cdot \beta B N^2 + 4\Gamma G_m P_{avg} - \frac{4P_{avg}}{C'} \cdot \frac{1}{\tau_p} . \tag{3.10}$$

A small perturbation $v_j \cdot \exp(j\omega t)$ should be superimposed to the steady state solution of rate equation to construct a small signal equivalent circuit model at the given externally applied bias voltage, i.e., $V(t) = V_0 + v_j \cdot \exp(j\omega t)$, and let

$$I(t) = I_0 + i \cdot \exp(\ j\omega t) , \tag{3.11}$$

$$N(t) = N_0 + n \cdot \exp(\ j\omega t) , \tag{3.12}$$

$$G_m(t) = G_{m0} + g_m \cdot \exp(\ j\omega t) , \tag{3.13}$$

$$S(t) = S_0 + s \cdot \exp(\ j\omega t) , \tag{3.14}$$

$$P_{avg}(t) = P_{avg\,0} + \Delta p \cdot \exp(\ j\omega t) , \tag{3.15}$$

where I_0, N_0, G_{m0}, S_0, and P_{avg0} are the respective steady state solutions of the rate equations and the optical gain equation. Some are presented in the previous chapter 2.3.

Equation 3.6 can be transformed into the equation below using Equations 3.11-3.15:

$$I + i \cdot \exp(j\omega t) = qN_w Wd \cdot LB(N_0^2 + n^2 \cdot \exp(j\omega t) + 2N_0 n \cdot \exp(j\omega t)) + \frac{4qL\Gamma}{E_{ph}} \cdot (G_{m0} + g_m \cdot \exp(j\omega t)) \times (P_{avg0} + \Delta p \cdot \exp(j\omega t)) + j\omega C_n \cdot v_j \cdot \exp(j\omega t) . \quad (3.16)$$

By neglecting higher order terms in the above equation, only the terms that include exp($j\omega t$) remain and are summarized as follows:

$$i \cdot \exp(j\omega t) = qN_w Wd \cdot LB \cdot 2N_0 n \cdot \exp(j\omega t) + \frac{4qL\Gamma}{E_{ph}} P_{avg0} g_m \cdot \exp(j\omega t) + \frac{4qL\Gamma}{E_{ph}} G_{m0} \Delta p \cdot \exp(j\omega t) + j\omega C_n v_j \cdot \exp(j\omega t) . \quad (3.17)$$

By omitting the exponential term exp($j\omega t$), the above equation can be written as

$$i = 2qN_w LWd \cdot BN_0 n + \frac{4qL\Gamma}{E_{ph}} \left(P_{avg0} g_m + G_{m0} \Delta p\right) + j\omega C_n v_j . \quad (3.18)$$

Further simplification is possible with the introduction of new parameters,

$$G_{sp} \equiv qN_w LWd , \quad (3.19)$$

$$G_{st} \equiv \frac{4qL\Gamma}{E_{ph}} . \quad (3.20)$$

Thus Equation 3.18 can be written as

$$j\omega C_n v_j = i - 2G_{sp} BN_0 n - G_{st} \left(P_{avg0} g_m + G_{m0} \Delta p\right). \quad (3.21)$$

To derive a lumped-element small signal equivalent circuit model, several theoretical components should be defined as

$$R_{s1} \equiv \frac{1}{\left(G_{st} P_{avg\,0} \left. \frac{dG_m}{dV_j} \right|_{v_j = v_{j0}} \right)} = \frac{1}{\left(\frac{4qL\Gamma}{E_{ph}} \cdot \frac{(N_w W d) E_{ph} C'}{4} S \cdot \left. \frac{dG_m}{dV_j} \right|_{v_j = v_{j0}} \right)}$$

$$= \frac{1}{\left(qL\Gamma N_w W d C' S \cdot \left. \frac{dG_m}{dV_j} \right|_{v_j = v_{j0}} \right)}, \tag{3.22}$$

$$R_{s2} \equiv \frac{1}{\left(2G_{sp} B N_0 \left. \frac{dN}{dV_j} \right|_{v_j = v_{j0}} \right)} = \frac{1}{\left(2qN_w LWd \cdot B N_0 \left. \frac{dN}{dV_j} \right|_{v_j = v_{j0}} \right)}, \tag{3.23}$$

$$g' \equiv G_{st} \cdot G_{m0} = \frac{4qL\Gamma}{E_{ph}} \cdot G_{m0}, \tag{3.24}$$

$$\alpha_{sp} \equiv \frac{\beta \cdot E_{ph}}{qL}, \tag{3.25}$$

$$\alpha_{st} \equiv \frac{E_{ph}}{qL}, \tag{3.26}$$

$$R_l \equiv \frac{C' \cdot \tau_p}{4}, \tag{3.27}$$

$$C_{op} \equiv \frac{4}{C'} \cdot \tag{3.28}$$

The average loss and the photon storage effect in the Fabry-Perot resonator structure are represented with R_l and C_{op}, respectively.

Using Equations 3.22-3.24, Equation 3.21 can be written as

$$j\omega C_n v_j = i - g' \cdot \Delta p - \frac{v_j}{R_{s1}} - \frac{v_j}{R_{s2}}. \tag{3.29}$$

Similarly, Equation 3.10 can be expressed by applying Equations 3.22-3.28 as

$$\frac{4}{C'} \cdot j\omega \Delta p \cdot \exp(j\omega t) = (N_w W d E_{ph}) \cdot \beta B \cdot \left(2N_0 n \cdot \exp(j\omega t)\right)$$

$$+ 4\Gamma G_{mo} \Delta p \cdot \exp(j\omega t) + 4\Gamma P_{avgo} \Delta p \cdot \exp(j\omega t)$$

$$- \frac{4\Delta p \cdot \exp(jwt)}{C'} \cdot \frac{1}{\tau_p}. \tag{3.30}$$

After removing common term exp($j\omega t$) and using the definitions 3.25-3.28, Equation (3.29) can be rearranged and simplified as

$$C_{op} \cdot j\omega \Delta p = \alpha_{sp} \cdot \Delta i_{sp} + \alpha_{st} \cdot \Delta i_{st} - \frac{\Delta p}{R_l}, \tag{3.31}$$

where

$$\Delta i_{sp} = 2G_{sp} B N_0 n = 2G_{sp} B N_0 v_j \times \left.\frac{dN}{dV_j}\right|_{v_j = v_{j0}} = \frac{v_j}{R_{s2}}, \tag{3.32}$$

$$\Delta i_{st} = G_{st}\left(G_{m0} \cdot \Delta p + g_m \cdot P_{avg\,0}\right) \tag{3.33}$$

$$= G_{st} \cdot G_{m0} \cdot \Delta p + G_{st} \cdot P_{avg\,0} \cdot v_j \times \left.\frac{dG_m}{dV_j}\right|_{v_j = v_{j0}} \tag{3.34}$$

$$= g' \cdot \Delta p + \frac{v_j}{R_{s1}}. \tag{3.35}$$

Finally, a scalable small-signal equivalent circuit model for quantum well lasers can be obtained from Equation 3.29 and 3.31. Before presenting the equivalent model, cavity length scalable components should be defined and summarized (Table 3.4).

Table 3.4 Cavity length scalable equivalent circuit model components summary.

Component	Description	Scale factor
R_b	Series resistor	$\times 1$
C_d	Depletion and diffusion capacitance	$\times L$
R_d	Depletion and diffusion resistor	$\times \frac{1}{L}$
C_n	Charge storage effect	$\times L$
R_{s2}	$\equiv \frac{1}{\left(2qN_w LWd \cdot BN_0 \left. \frac{dN}{dV_j} \right\|_{v_j = v_{j0}} \right)}$	$\times \frac{1}{L}$
R_{s1}	$\equiv \frac{1}{\left(qL\Gamma N_w WdC'S \cdot \left. \frac{dG_m}{dV_j} \right\|_{v_j = v_{j0}} \right)}$	$\times \frac{1}{L}$
g'	$\equiv \frac{4qL\Gamma}{E_{ph}} \cdot G_{m0}$	$\times L$
α_{sp}	$\equiv \frac{\beta \cdot E_{ph}}{qL}$	$\times \frac{1}{L}$
α_{st}	$\equiv \frac{E_{ph}}{qL}$	$\times \frac{1}{L}$
R_l	$\equiv \frac{C' \cdot \tau_p}{4}$	$\times 1$
C_{op}	$\equiv \frac{4}{C'}$	$\times 1$
α_l	Intrinsic loss	$\times 1$

3.3.4.2 Circuit Implementation and Simulation Results

By applying the introduced cavity-length scalable factor L, Equations 3.29 and 3.31 can construct a scalable small-signal equivalent circuit laser diode model for the use of general nodal circuit simulators such as Spice and Agilent ADS®. Figure 3.30 shows the obtained cavity-length scalable small-signal equivalent circuit model for multiple quantum well laser diodes, and Figure 3.31 presents the actual schematic implementation using the commercial circuit simulator ADS®.

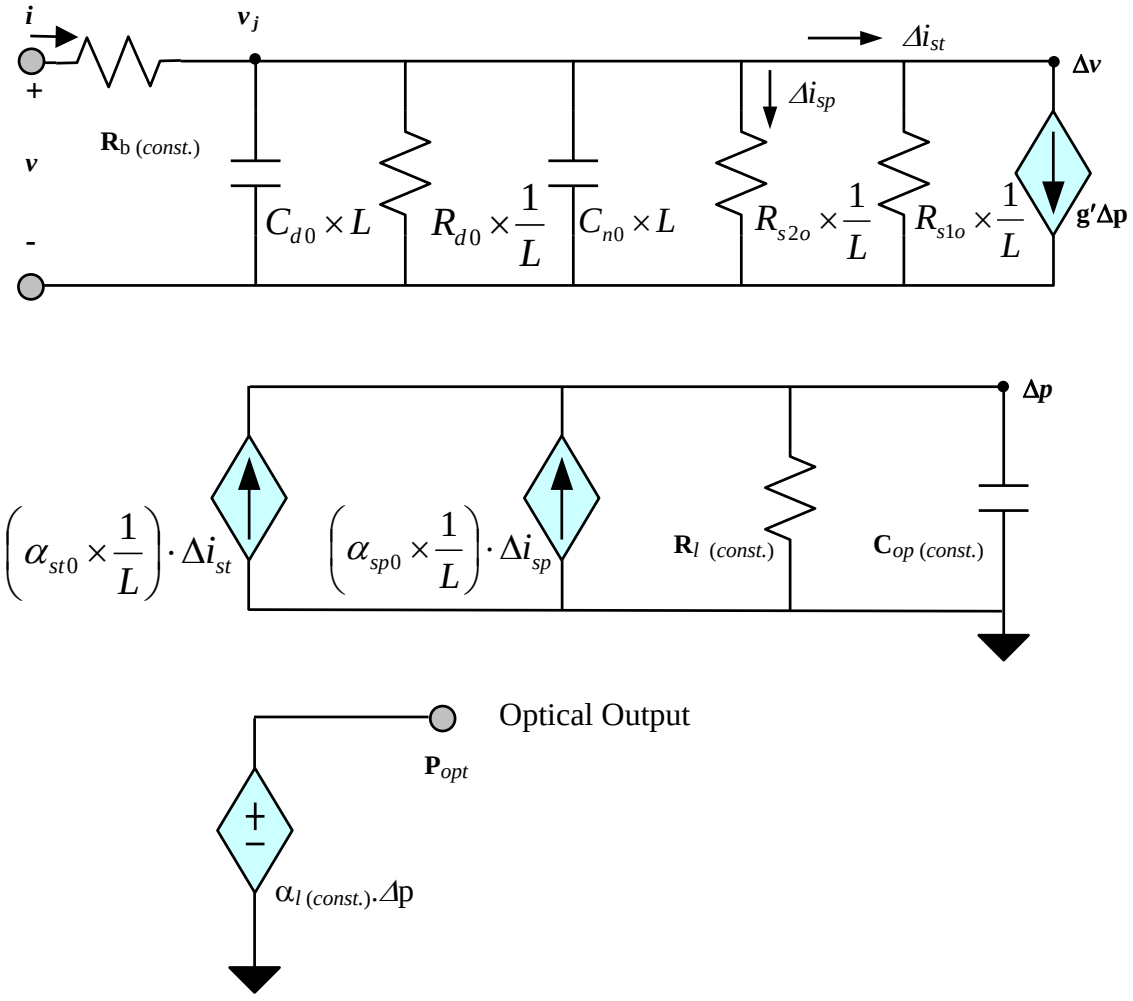

Figure 3.30 Theoretically derived cavity-length scalable laser diode small-signal circuit model.

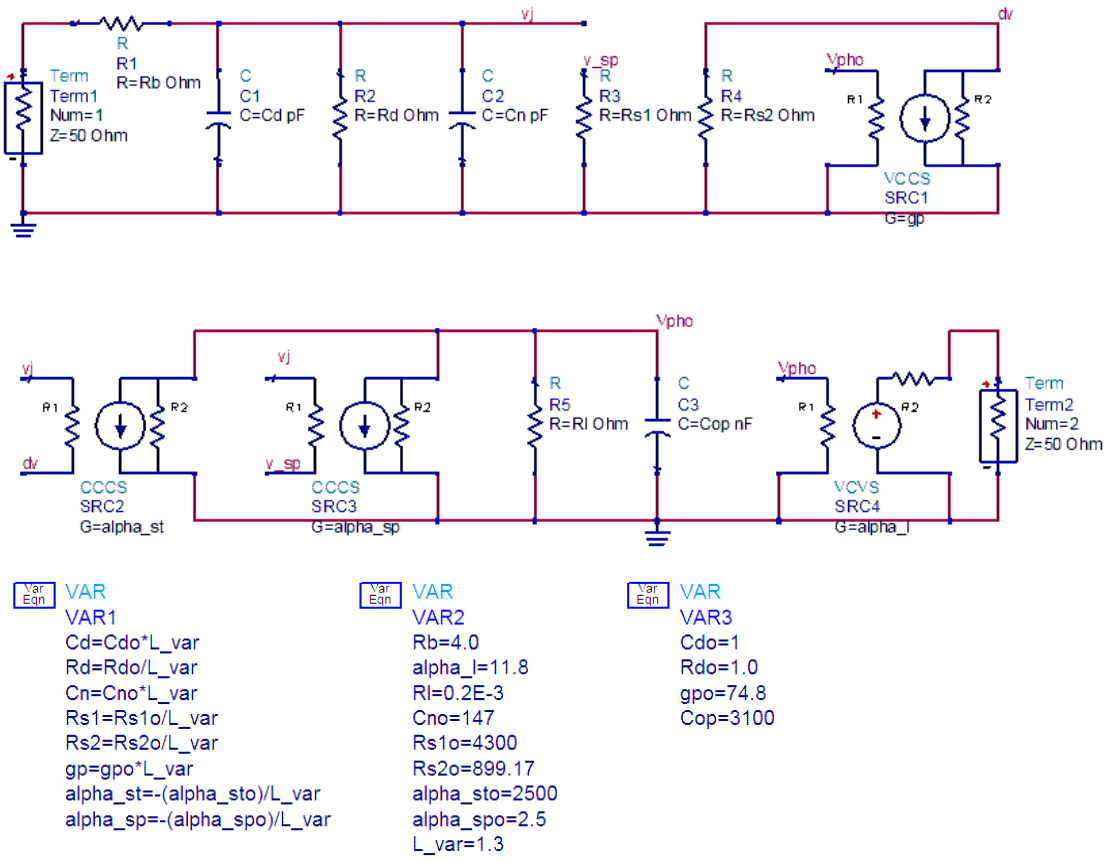

Figure 3.31 The actual schematic implementation for the theoretically derived scalable circuit model.

The cavity length dependent circuit components are included in the variable definitions at the bottom of Figure 3.31. Changing the parameter L_var value can control the length of the nominated cavity length. For example, defining L_var=1.3 implements a 30 % increase to the cavity length.

The electrical-to-optical conversion response for the nominated cavity length is shown in Figure 3.32, and the parameters for the derived equivalent circuit model are given in Table 3.5.

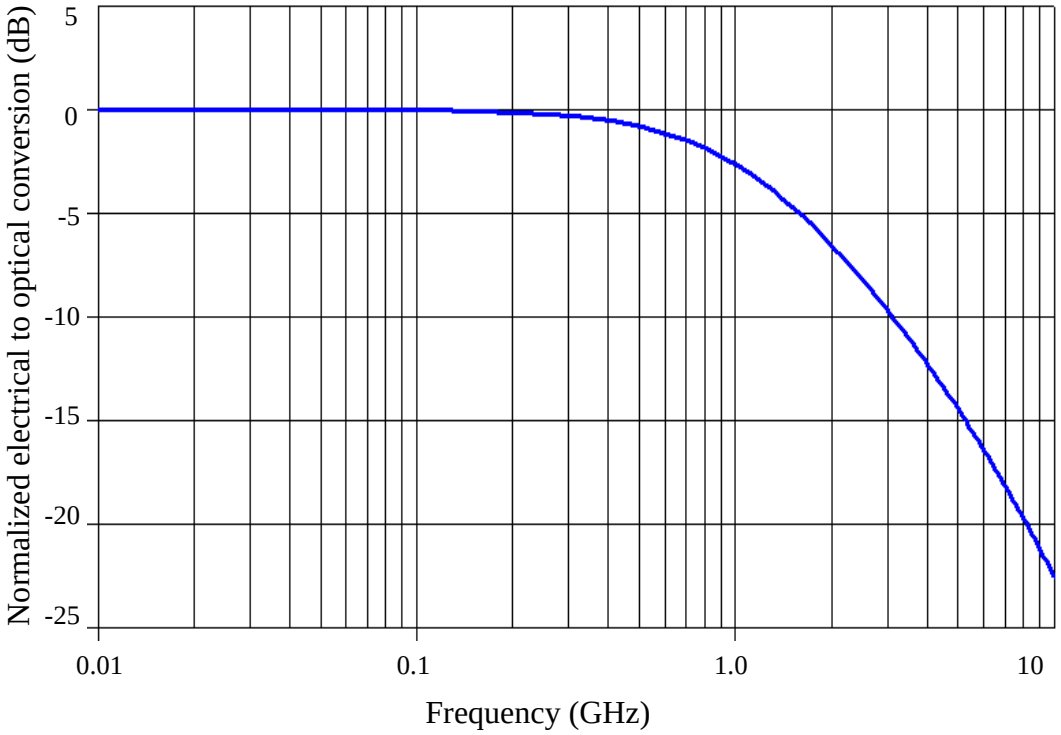

Figure 3.32 **The electrical-to-optical conversion response of the theoretically derived circuit model with no change of the nominated cavity length,**

Table 3.5 **Parameters for the theoretically derived equivalent circuit model.**

Parameter	Description	Value
R_b	Series resistor	4 Ω
B	Radiative recombination coefficient	3.4×10^{-11} cm^3s^{-1}
β	Coupling coefficient	1.0×10^{-3}
R	Reflectivity	0.3
Γ	Mode confinement factor	0.187
α_l	Intrinsic loss	11.8 cm^{-1}

Using this theoretically derived scalable laser diode circuit model, the electrical-to-optical conversion responses are simulated along the different cavity lengths. The extent of cavity length changes should be confined within ± 20% or ± 30% variation to secure linear shifts of the device performances. Excessive cavity length variation from the designated value may require non-linear modeling approaches. Figure 3.33 shows the electrical-to-optical conversion performance changes along ± 30% cavity length variations.

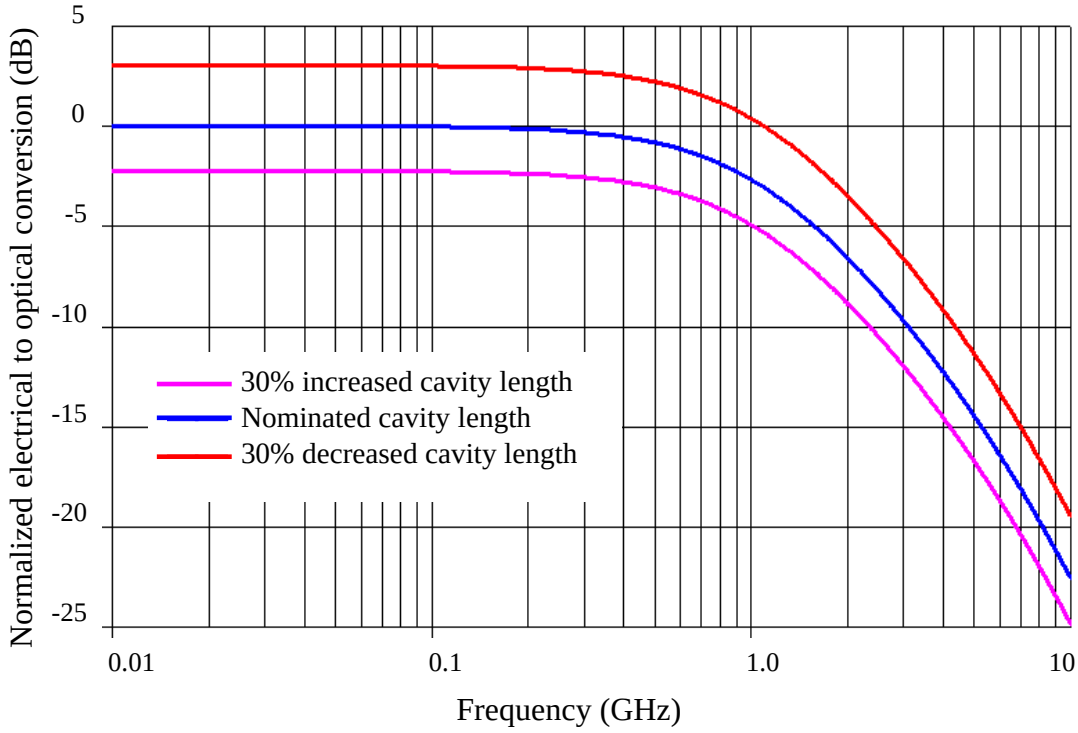

Figure 3.33 The electrical-to-optical conversion response of the theoretically derived circuit model with 3 different cavity lengths.

3.3.4.3 Effectiveness Demonstration of the Building Block-Based Scalable Laser Model

The basic concept of the building block-based scalable model is presented in Chapter 3.3.2. The total circuit shown in Figure 3.34 is composed of 13 identical building blocks. Device scaling is achieved by the addition or elimination of the basic building block that is enclosed by the black rectangle in the first row of the figure. For example, the structure that is obtained by removing both "section A" and "section B" corresponds to 30% cavity length decrease, and the structure by removing only one section corresponds to the nominated cavity length.

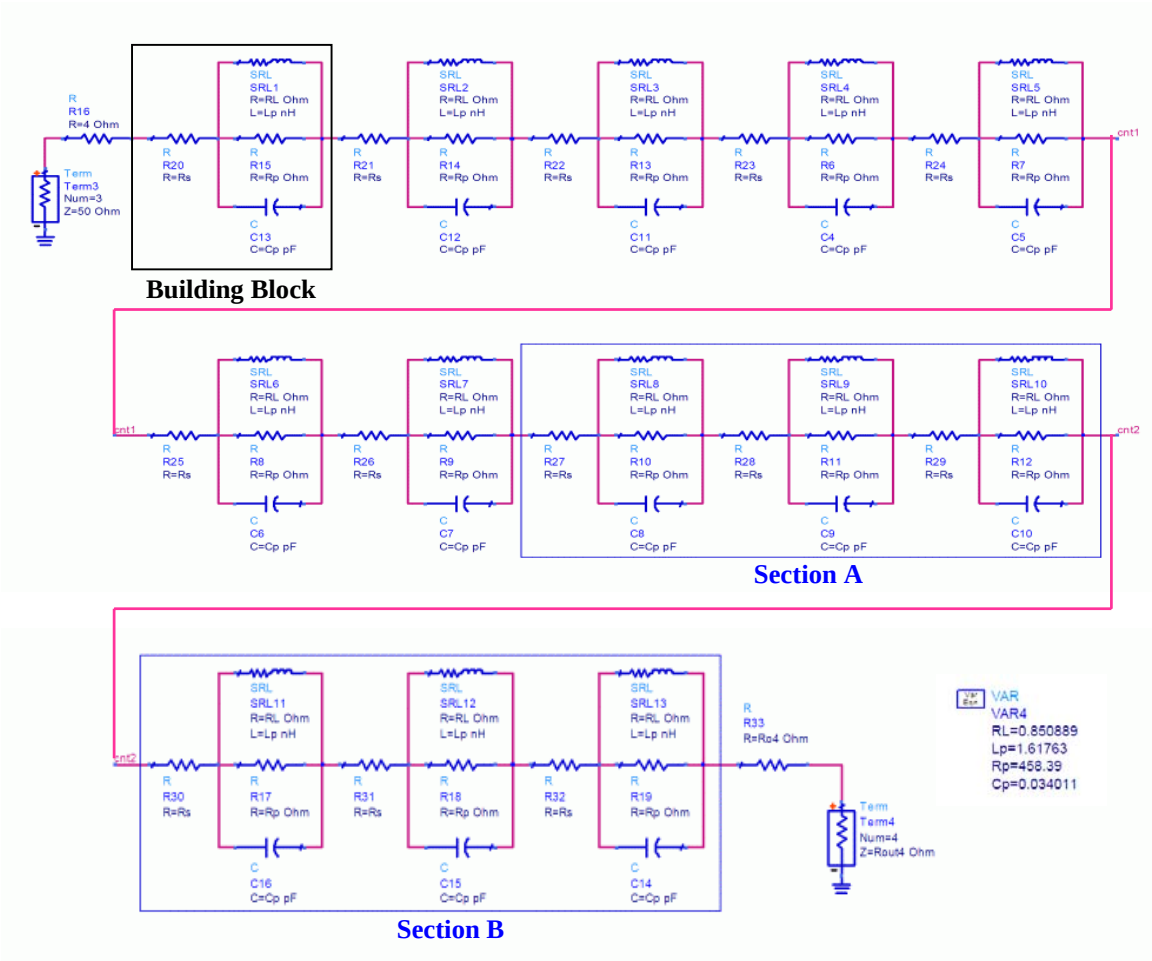

Figure 3.34 The schematic of the building block-based scalable laser diode equivalent circuit.

The process of fitting the scalable model to the simulated scattering parameters from the numerically derived scalable rate equation is explained as follows. First, the electrical to optical transfer response from the selected building block should have a similar trajectory with the derived rated equation model response. If this condition is not met, then additional cascading of the ill-chosen building blocks cannot construct a well predicting model. Second, reasonable initial values should be assigned to the basic building block. The first resonant frequency of the derived rate equation model can give a rough boundary on the approximate values of inductance and capacitance in the selected building block. This initial guess is also important for optimization time. In addition, a poor initial guess can cause nonphysical values like negative inductance or capacitance. Third, the number of building blocks should be decided according to the range of cavity length variation. For example, ten building blocks in Figure 3.34 were chosen to express the nominated cavity length laser, therefore adding or deleting one building block can express 10% length increase or decrease. If narrower step size such as a 5% variation is needed, the number of building blocks should increase. Because large length variation in real-world laser diodes can lead to non-linear variation of performances, a proper boundary limitation should be given on the cavity length change. Fourth, the optimization to the nominated cavity length is conducted, and then scalability is checked with adding or deleting basic building blocks at the shortest or longest cavity length. It should be remembered in the optimization process that the components values in each block are identical. Finally, if needed, a parasitic block can be included in the constructed scalable equivalent model.

In this chapter, the effectiveness of the building block modeling approach is demonstrated by the comparison of the numerically derived scalable rate equation result and the building block-based scalable laser model simulation result. Figure 3.35 shows their normalized electrical-to-optical simulation results.

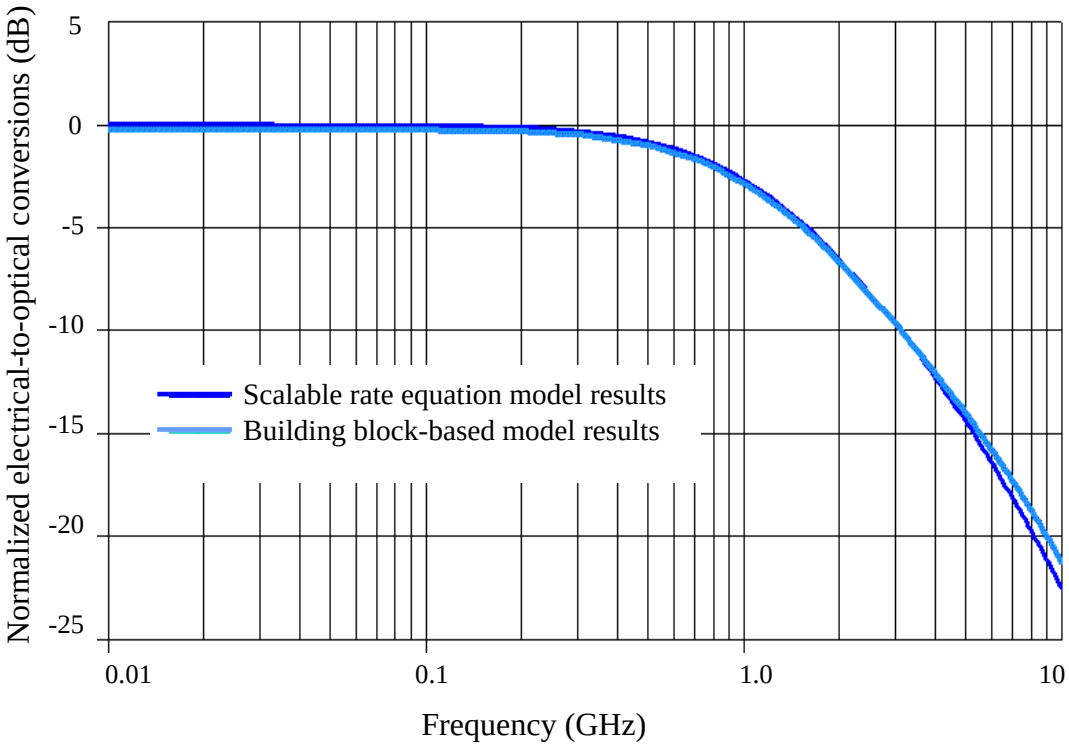

Figure 3.35 The electrical-to-optical conversion responses of the theoretically derived circuit model simulation and building block-based model simulation with the nominated cavity length.

The simulated response with the proposed building block-based model shows a good agreement with the obtained result using the scalable rate equation model. It is important to prove that the building block-based model can predict the given laser diode performance variation along the change of cavity length by adding or eliminating the number of building blocks. The effectiveness of this building block model is confirmed in Figures 3.36 and 3.37.

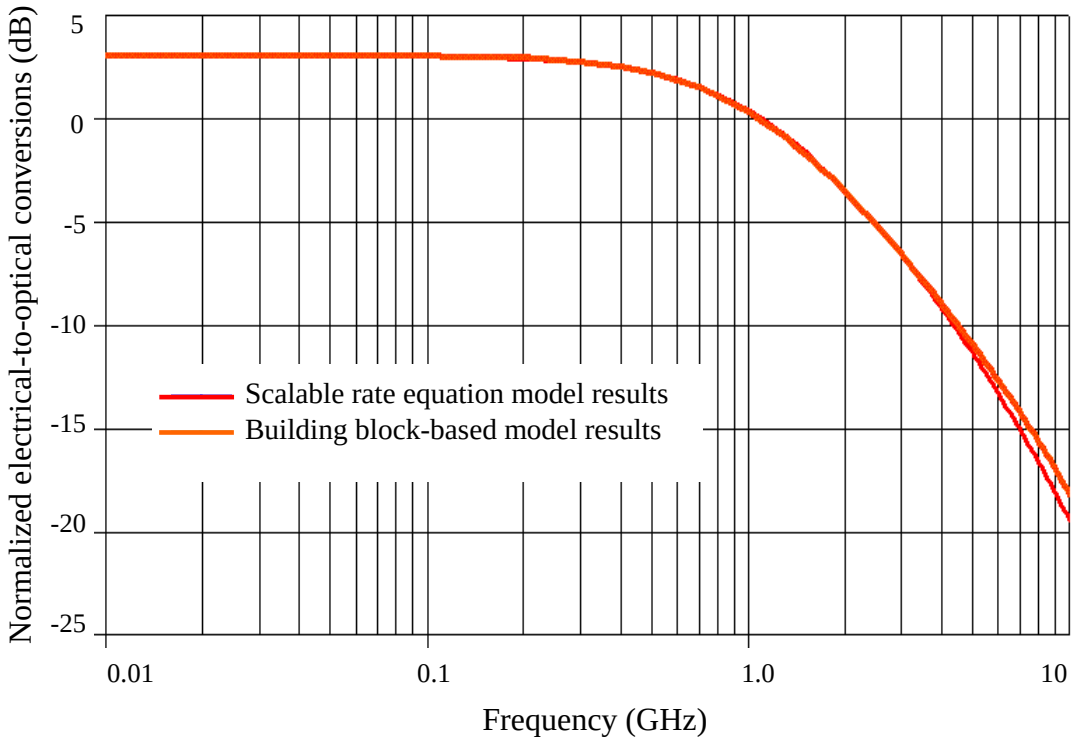

Figure 3.36 The electrical-to-optical conversion responses of the theoretically derived circuit model simulation and building block-based model simulation with a 30% cavity length decrease,

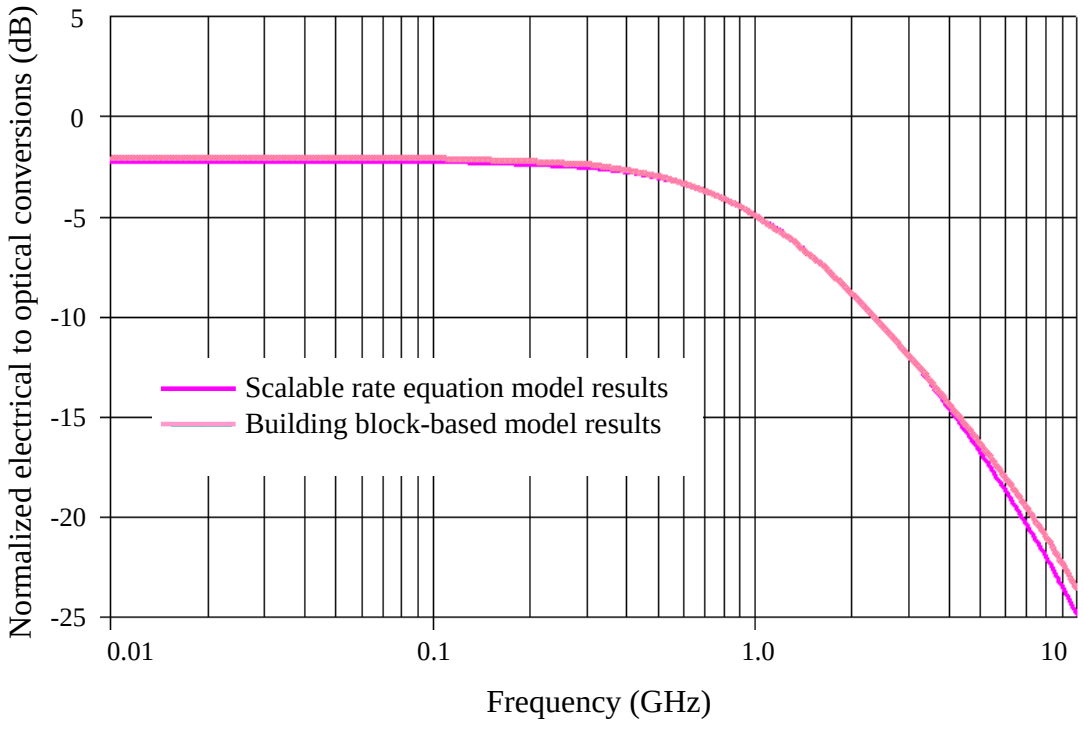

Figure 3.37 The electrical-to-optical conversion responses of the theoretically derived circuit model simulation and building block-based model simulation with a 30% cavity length increase.

3.3.5 The Model Application for the Circuit Design

3.3.5.1 Laser Drive Circuit Design for an Optical Transmitter

The simple optical transmitter circuits, such as a single-ended laser driver and differential type laser driver, were discussed and simulated in Section 3.2.4. For simplicity, high-performance broadband transistors were selected to not interfere with the comparison of the performance difference between the proposed multiple-resonance model and the conventional model. For many applications, this situation is very unusual in that the use of high-performance devices increases product cost directly. Transistor models with a reasonable bandwidth budget should be used in the real circuit simulation and implementation in this regard.

3.3.5.2 Performance Optimization through the Laser Diode Scaling

After obtaining a reasonable scalable equivalent circuit model for the fabricated laser diodes and selecting an appropriate optical transmitter topology, overall optical transmitter performance can be simulated and optimized by changing available circuit parameters. Especially, laser diode scaling will be used for the circuit performance enhancement. The optimization goal could be maximum operating frequency, low power consumption, or maximum electrical-to-optical (E/O) transfer gain. Achieving a wide opened eye-diagram (as an optimization goal) could be a meaningful starting point.

Chapter 4. Conclusion

In the case of a commercial discrete laser diode modeling, the proposed wide-band multiple-resonance lumped element small-signal laser circuit model showed remarkable accuracy in simulation. Particularly, the proposed model could express two important factors in laser diode performance such as electrical-to-optical conversion and input return loss at the same time. Eye-diagram simulation in time domain also validated its effectiveness.

Unfortunately, in scalable laser diode modeling, the fabricated lasers failed to show reliable performances: thus, we derived a scalable rate equation-based circuit model by using numerical analysis. As our goal is to show that the proposed scalable model can predict the performance change along device scaling, applying theoretical device instead of using a real device can be justified. The proposed building block-based laser diode modeling approach also demonstrated reliable simulation results.

As the proposed laser diode models offered fast and reliable simulation capability, the results show that we can improve the accuracy of optoelectronic circuit design by using these proposed models.

REFERENCES

[1] U. Koren, B. Miller, Y. Su, T. L. Koch, and J. E. Bowers, "Low internal loss separate confinement heterostructure InGaAs/InP quantum well laser," Applied Physics Letters, vol. 51, pp. 1744-1746, 1987.

[2] A. Kasukawa, I. Imajo, and T. Makino, "1.3 μm GaInAsP/InP GRIN-SCH-MQW laser diodes grown by MOCVD," Electronic Letters, vol. 25, pp. 104-105, 1989.

[3] T. L. Koch, U. Koren, R. P. Gnall, C. A. Burrus, and B. I. Miller, "Continuously tunable 1.5 μm MQW-DBR lasers," Electronic Letters, vol. 24, pp. 1431-1432, 1988.

[4] P. Diament, Wave Transmission and Fiber Optics, Macmillan, New York, 1990.

[5] S. C. Javro and S. M. Kang, "Transforming Tucker's linearized laser rate equations to form that has a single solution regime," Journal of Lightwave Technology, vol. 13, no. 9, pp. 1899-1904, 1995.

[6] L. V. T. Nguyen, A. J. Lowery, P.C. R. Gurney, and D. Novak, "A time domain model for high-speed quantum well lasers including carrier transport effects," IEEE Journal of Selected Topics in Quantum Electronics, vol. 1, no. 2, pp. 494-504, 1995.

[7] SILVACO International, 4701 Patrick Henry Drive, Building 1, Santa Clara, CA 95054, "ATLAS User's Manual," vol. 1, 2000.

[8] G. Song, K. Hess, T. Kerkhoven, U. Ravaioli, "Two-dimensional simulator for semiconductor lasers," Electron Device Meeting, pp. 143-146, Dec. 1989.

[9] B. Witzigmann, A. Andreas, and W. Fichtner, "A multidimensional laser simulator for edge-emitters including quantum carrier capture," IEEE Transactions on Electron Devices, vol. 47, no. 10, pp. 1926-1934, 2000.

[10] D. Wilt and A. Yariv, "A self-consistent static model of the double-heterostructure laser," IEEE Journal of Quantum Electronics, vol, QE-17, pp. 1941-1951, 1981.

[11] S. Seki, M. Tomizawa, K. Yokoyama, and Y. Yoshii, "Two-dimensional, static, and dynamic device simulation of laser diodes," Proc. CLEO, 1988.

[12] D. Scharfetter and H. Gummel, "Large-signal analysis of a silicon read diode oscillator," IEEE Transactions on Electron Devices, vol. ED-16, pp. 64-77, Jan. 1969.

[13] T. Simlinger, H. Brech, T. Grave, and S. Selberherr, "Simulation of submicron doble-heterojunction high electron mobility transistors with MINIMOS-NT," IEEE Transaction on Electron Devices, vol. 44, pp. 700-707, May 1997.

[14] Y. Apanovich et al., "Numerical simulation of submicrometer devices including coupled nonlocal transport and nonisothermal effects," IEEE Transactions on Electron Devices, vol. 42, pp. 890-898, May 1995.

[15] C. Ho, A. Ruehli, and P. Brennan, "The modified nodal approach to network analysis," IEEE Transactions on Circuits and Systems, vol. 22, no. 6, pp. 504-509, June 1975.

[16] F. Chang, "The unified nodal approach to circuit analysis," IEEE International Symposium on Circuits and Systems, vol. 2, pp. 849-852, June 1997.

[17] M. R. Salehi, B. Cabon, "Circuit modeling of quantum-well lasers for optoelectronic integrated circuits including physical effect of deep-level traps," IEEE Journal of Quantum Electronics, vol. 38, no. 11, pp. 1510-1514, 2002.

[18] S. Ghoniemy *et al*., "Robust semiconductor laser modeling for analog optical link simulations," in Proc. IEEE NUSOD, 2002.

[19] S. Ghoniemy, L. MacEachern, and S. Mahmoud, "Enhanced large signal laser modeling including thermal effects for analog communications," 4th laser and fiber-optical networks modeling, 2002. Proceedings of the 2002 Laser and Fiber-optical Networks Modeling, pp. 21-24, 2002.

[20] S. Ghoniemy, L. MacEachern, and S. Mahmoud, "Extended roubust semiconductor laser modeling for analog optical link simulations," IEEE Journal of Selected Topics in Quantum Electronics, vol. 9, no. 3, pp. 872-878, 2003.

[21] S. Min, "Automated Construction of Macromodels from Frequency Data for Simulation of Distributed Interconnect Networks," Ph.D. Thesis, Georgia Institute of Technology, May 2004.

[22] K. Choi and M. Swaminathan, "Development of model libraries for embedded passives using network synthesis," IEEE Transactions on Analog and Digital Signal Processing, vol. 47, no. 4, April 2000.

[23] K. Choi, "Modeling and simulation of embedded passives using rational functions in Multi-layered substrates," Ph.D. Thesis, Georgia Institute of Technology, August 1999.

[24] N. Na, "Modeling and simulation of planes in electronic packaging," Ph.D. Thesis, Georgia Institute of Technology, January 2001.

[25] W. Press, S. Teukolsky, W. Vetterling, and B. Flannery, "Numerical receipes in C: The art of scientific computing," 2nd Ed. Oxford, U.K., Cambridge Univ. Press, 1992.

[26] B. Gustavsen and A.Semlyen, "Rational approximation of frequency domain responses by vector fitting," IEEE Transactions on Power Delivery, vol. 14, no. 3, July 1999.

[27] L. Bjerkan, A. Royset, L. Hafskjaer, and D. Myhre, "Measurement of laser parameters for simulation of high-speed fiberoptic systems," Journal of Lightwave Technology, vol. 14, pp. 839-850, 1996.

[28] P. Mena, J. Morikuni, S. Kang, A. Harton, and K. Wyatt, "A comprehensive circuit-level model of vertical-cavity surface-emitting lasers," Journal of Lightwave Technology, vol. 17, no. 12, pp. 2612-2632, 1999.

[29] R. S. Tucker and D. J. Pope, "Microwave circuit models of semiconductor injection lasers," IEEE Transactions on Microwave Theory and Technology, vol. MTT-31, no. 3, pp. 289-294, 1983.

[30] C. R. Irving and J. E. Carroll, "An equivalent circuit model of a multimode semiconductor laser," IEE Colloquium on Modeling of Optoelectronic Devices, pp. 11/1-11/4, 1990.

[31] J. Lee, S. Nam, S. H. Lee, and J. Jeong, "A complete small-signal equivalent circuit model of a cooled butterfly-type 2.5 Gbps DFB laser modules and its application to improve high frequency characteristics," IEEE Transactions on Advanced Packaging, vol. 25, no. 4, pp. 543-548, 2002.

[32] C. Chun, A Pham, J. Laskar and B. Hutchison, "Development of microwave package models utilizing On-wafer characterization techniques," IEEE Transactions on Microwave Theory and Technology, vol. 45, pp. 1948-1954, 1997.

[33] E. Godshalk, "Characterization of surface mount packages at microwave frequencies using wafer probes," IEEE Microwave Theory and Technology Digest, pp. 1887-1890, 2000.

[34] M. Banu, B. Jalali, R. Nottenburg, D. A. Humphery, R. K. Montgomery, R. A. Hann, and M. B. Panish, "10 Gbit/s bipolar laser driver," Electronic Letters, vol. 27, pp. 278-280, 1991.

[35] H. M. Rein, E. Bertagnolli, A. Felder, and L. Schmidt, "Silicon bipolar laser and line driver IC with symmetrical output pulse shape operation up to 12 Gbit/s," Electronic Letters, vol. 28, no. 14, pp. 1295-1296, 1992.

[36] R. Poddar and M. Brooke, “Accurate High Speed Modeling of Integrated Passive Devices in Multichip Modules,” Proceeding of Electrical Performance of Electronic Packaging, pp. 184-186, 1996.

[37] L. A. Carastro, R. Poddar, E. Moon, M. Brooke, and N. Jokerst, “Passive device modeling methodology using nonlinear optimization,” Proceedings of the 1999 IEEE International Symposium on Circuits and Systems VLSI, vol. 6, pp. 53-56, 1999.

[38] R. Poddar, E. M. Moon, M. Brooke, and N. Jokerst, “Accurate, rapid, high frequency empirically based predictive modeling of arbitrary geometry planar resistive passive devices,” IEEE Transactions on Components, Packaging, and Manufacturing Technology, vol. 21, no 2, pp. 177-183, 1998.

[39] M. Yano, H. Imai, K. Hori, and M. Takusagawa, “High temperature characteristics of strip-geometry InGaAsP/InP double-heterostructure lasers,” IEEE Journal of Quantum Electronics, vol. 17, no. 5, pp. 619-626, 1981.

[40] C.-S. Li, F. F.-K. Tong, K. Liu, and D. G. Messerschmitt, “Channel capacity optimization of chirp-limited dense WDM/WDMA systems using OOK/FSK modulation and optical filters,” Journal of Lightwave Technology, vol. 10, no. 8, pp. 1148-1161, 1992.

[41] M. Majewski and D Novak, “Method for characterization of intrinsic and extrinsic components of semiconductor laser diode circuit model,” IEEE Microwave and Guided Wave Letters, vol. 1, no. 9, pp. 246-248, 1991.

[42] D. Gao *et al.*, “Modeling of QW lasers for computer aided analysis of optoelectronic integrated circuit,” IEEE Journal of Quantum Electronics, vol. 26, pp. 1206-1216, July 1990.